

**Measuring Surface Ocean Wave Height and
Directional Spectra Using an Acoustic Doppler
Current Profiler from an Autonomous Underwater
Vehicle**

by
Scott Haven

B.S. Oregon State University (2005)
Submitted to the Department of Mechanical Engineering
in partial fulfillment of the requirements for the degree of
Master of Science in Mechanical Engineering


at the
MASSACHUSETTS INSTITUTE OF TECHNOLOGY
and the
WOODS HOLE OCEANOGRAPHIC INSTITUTION

September 2012

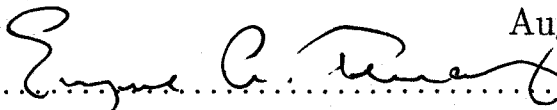
© 2012 Scott Haven

All Rights Reserved.

The author hereby grants to MIT and WHOI permission to reproduce and to distribute
publicly paper and electronic copies of this thesis document in whole or in part in any
medium now known or hereafter created.

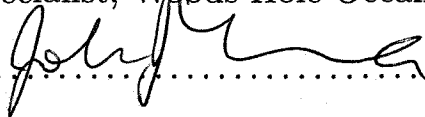
Author 
.....
Department of Mechanical Engineering

August 20, 2012

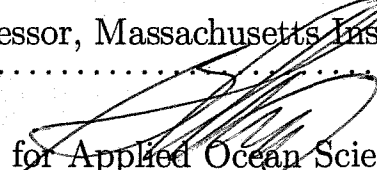
Certified by 
.....
Eugene A. Terray

Research Specialist, Woods Hole Oceanographic Institution


Thesis Supervisor

Reader 
.....
John J. Leonard

Professor, Massachusetts Institute of Technology

Accepted by 
.....
Henrik Schmidt

Chair, Joint Committee for Applied Ocean Science and Engineering

Accepted by 
.....
David E. Hardt
Chair, Committee on Graduate Students - Mechanical Engineering

Measuring Surface Ocean Wave Height and Directional Spectra Using an Acoustic Doppler Current Profiler from an Autonomous Underwater Vehicle

by

Scott Haven

Submitted to the Department of Mechanical Engineering
on August 20, 2012, in partial fulfillment of the
requirements for the degree of
Master of Science in Mechanical Engineering

Abstract

The Acoustic Doppler Current Profiler (ADCP) is a proven technology which is capable of measuring surface wave height and directional information, however it is generally limited to rigid, bottom mounted applications which limit its capabilities for measuring deep water waves. By employing an upward looking ADCP on a moving platform, such as an autonomous underwater vehicle or submerged float, we show that it is possible to remove the wave induced motion of the platform and accurately measure surface ocean wave information.

The platform selected for testing was a REMUS-100 vehicle equipped with an upward and downward looking ADCP and high accuracy Kearfott inertial navigation unit. Additionally, a Microstrain 3DM-GX3-25 Attitude Heading Reference System was tested as a low cost alternative to the Kearfott system. An experiment consisting of multiple REMUS deployments was conducted near the Martha's Vineyard Coastal Observatory (MVCO). The wave induced motion was measured by various inertial and acoustic sensors and removed from the ADCP data record. The surface wave height and mean directional estimates were compared against a Datawell MKIII directional Waverider buoy and bottom mounted 1200 kHz upward looking ADCP at the MVCO.

Results demonstrate that the non-directional spectrum of wave height and the mean wave direction as a function of frequency can be accurately measured from an underway autonomous underwater vehicle in coastal depth waters using an ADCP.

Thesis Supervisor: Eugene A. Terray

Title: Research Specialist, Woods Hole Oceanographic Institution

Acknowledgments

I would first like to give my most sincere thanks to my thesis advisor, Dr. Gene Terray. Without his superb technical guidance, expertise, and experience, this thesis would have never been possible. Thank you.

I am also equally thankful to my good friend and lunch partner, Ryan Gielegem. While Gene might have got me through my thesis, Ryan got me through MIT. He is one of the smartest guys that I have ever worked with and was always willing to go over topics with me to make sure I understood what was going on. Thanks buddy.

I would like to give a big thanks to the everyone who helped me get a REMUS vehicle ready for missions and in the water. Mike Purcell, Amy Kukulya, and Robin Littlefield always went out of their way to make sure a vehicle was ready and that I got the best data possible. Roger Stokey and Gwyneth Packard spent countless hours integrating a challenging new sensor into the REMUS and were always willing to answer questions and make changes when I needed it.

Thanks to Ken Houltter and Ian Hanley from the R/V *Tioga*. I truly appreciate their flexibility and willingness to go out in bad seas to support my operations.

I would also like to thank Dr. John Leonard from MIT for ensuring that I was always on the right path academically. Thanks to Dr. Hanu Singh for getting me on the right path as soon as I showed up to Woods Hole and for getting me excited about research and the possibilities. Thanks to Geoff Gorman for being the senior guy and acting as an informal advisor and more importantly, a good friend to me and my family.

I truly appreciate the program entrance recommendations and guidance that I received from CAPT Chris Anklam, CDR Trent Hesslink, CDR Steven Hall, and LCDR Geoff Patterson. The mentorship and leadership that these men showed me I truly believe helped me to succeed at this challenging institution.

My family and I would like to thank Martin, Kate, and Eli Roschmann for their friendship, support, and unending wit. The time we spent with them served as our escape from the intensity and challenges of MIT and always helped to refuel my

interest in academia and my research.

Finally, I would like to thank the U.S. Navy, Woods Hole Oceanographic Institute, and the Woods Hole Oceanographic Institute's "Access to the Sea" program for sponsoring my education and research and for providing me with a truly once in a lifetime experience.

Thank you.

Dedication

This thesis is dedicated to my family. Without the unyielding support of my parents and sisters, and the love and dedication of my wife, Marisa, and my son, Charlie, not only would I not have been able to do this, but I would have no one to do it for. You all are truly my inspiration and I love all of you.

Contents

1	Introduction	17
1.1	Motivation	17
1.2	Objectives	18
1.3	History of Ocean Wave Spectral Analysis	19
1.4	Recent AUV Wave Research Efforts	20
1.5	Overview of Study	20
2	Acoustic Doppler Current Profiler	23
2.1	Introduction	23
2.2	ADCP History	23
2.3	Theory of Operation	24
2.3.1	The Doppler Effect	24
2.3.2	Range Gating	24
2.3.3	ADCP Coordinate Frame	25
2.4	ADCP Wave Analysis	27
2.4.1	Linear Wave Theory	28
2.4.2	Surface Spectrum Analysis	29
2.4.3	Wave Height Analysis	29
2.4.4	Wave Direction Analysis	30
2.4.5	Error in the Mean Direction Estimate	31
3	Experiment	33
3.1	Introduction	33

3.2	Funding	34
3.3	Equipment and Sensors	34
3.3.1	Martha’s Vineyard Coastal Observatory	34
3.3.2	REMUS-100	35
3.3.3	Datawell Waverider Buoy	38
3.4	Logistics and Mission Planning	41
3.4.1	April 20th 2012	42
3.4.2	April 26th 2012	43
3.4.3	May 17th 2012	44
3.4.4	July 27th 2012	45
4	Signal Processing	47
4.1	Introduction	47
4.2	Correlation of Sensors	48
4.2.1	3DM and Kearfott Correlation	48
4.2.2	ADCP and Kearfott Correlation	48
4.3	REMUS ADCP	49
4.3.1	REMUS ADCP Processing Method	50
4.4	Kearfott INU	51
4.4.1	Kearfott Processing Method	53
4.5	Microstrain 3DM-GX3-25	53
4.5.1	3DM Processing Method	54
4.6	MVCO ADCP	55
4.6.1	MVCO Processing Method	56
4.7	Datawell Waverider Buoy	57
4.7.1	Datawell Processing Method	57
4.8	Doppler Correction	58
5	Sensor Comparison and Analysis	61
5.1	Introduction	61
5.2	Sensor to Sensor Data Comparisons	61

5.2.1	3DM to Kearfott	62
5.2.2	ADCP to Kearfott	66
5.3	Spectral Comparison	67
5.3.1	Height Spectra	68
5.3.2	Mean Wave Direction	69
6	Summary and Conclusions	73
6.1	Summary	73
6.2	Future Work	74
6.2.1	Environmental Work	75
6.2.2	Wavelet Analysis	75
6.2.3	Subsurface Moorings	75
6.2.4	Naval Submarine Employment	76
6.3	Conclusion	77
A	The Doppler Effect	79
A.1	Introduction	79
A.2	Derivation	79
A.3	ADCP Application	81
B	Water Wave Mechanics	83
B.1	Introduction	83
B.2	Linear Wave Theory	83
B.2.1	The Laplace Equation	84
B.2.2	Boundary Conditions	85
B.2.3	Solution of the Boundary Value Problem	86
B.3	Random Wave Theory	88
B.3.1	Wavenumber Spectrum	88
B.3.2	Directional Wave Spectrum	89
C	Spectral Analysis	91
C.1	Introduction	91

C.2	Height Spectra Analysis	91
C.3	Mean Wave Direction Analysis	93
D	Mission Results and Data	95
D.1	Mission Results and Comparison	95
D.1.1	April 20th 2012	95
D.1.2	April 26th 2012	96
D.1.3	May 17th 2012	99
D.1.4	July 27th 2012	101
E	Additional Sensor Comparison Results	105
E.1	Introduction	105
E.2	3DM to Kearfott Accelerometers	105
E.3	3DM to Kearfott Angular Rates	106
E.4	3DM to Kearfott Euler Angles	107
E.5	3DM to Kearfott Vehicle Velocities	108
E.6	ADCP Bottom Track to Kearfott Vehicle Velocities	110
F	Microstrain Complementary Filter and Noise Analysis	111
F.1	Introduction	111
F.2	Complementary Filter	111
F.3	Sensor Noise and Error	112
F.4	Static Lab Noise Analysis	113
F.5	Field Data Noise Analysis	114

List of Figures

2-1	ADCP Range Gating	25
2-2	ADCP Instrument Coordinate Frames	27
3-1	Martha’s Vineyard Coastal Observatory	35
3-2	REMUS-100	36
3-3	3DM-GX3-25	38
3-4	Datawell MKIII Directional Waverider Buoy	39
3-5	Datawell MKIII Directional Waverider Buoy Mooring System	40
3-6	WHOI Research Vessel <i>Tioga</i>	42
3-7	REMUS Mission Path April 20th 2012	43
3-8	REMUS Mission Path and Bathymetry April 26th 2012	44
4-1	Kearfott and Microstrain Correlation	49
4-2	ADCP and Kearfott Correlation	50
4-3	Uncorrected Height and Mean Wave Direction Example	52
4-4	Bottom Track Corrected Height and Mean Wave Direction Example	52
4-5	Kearfott Corrected Height and Mean Wave Direction Example	53
4-6	Microstrain Corrected Height and Mean Wave Direction Example	55
4-7	MVCO Height and Mean Wave Direction Example	56
4-8	Datawell Waverider Buoy Height and Mean Wave Direction Example	58
4-9	Doppler Correction	60
5-1	Raw 3DM and Kearfott Accelerations	63
5-2	Raw 3DM and Kearfott Angular Rates	64

5-3	3DM and Kearfott Heading	65
5-4	3DM and Kearfott Forward Velocity	66
5-5	Kearfott and ADCP Bottom Track Velocities	67
5-6	April 26th Height Spectrum Comparison	68
5-7	May 17th Height Spectrum Comparison	69
5-8	July 27th Height Spectrum Comparison	70
5-9	April 26th Mean Wave Direction Comparison	70
5-10	May 17th Mean Wave Direction Comparison	71
5-11	July 27th Mean Wave Direction Comparison	72
A-1	The Doppler Effect	80
D-1	April 26th Height Spectra	97
D-2	April 26th Mean Wave Direction	98
D-3	May 17th Height Spectra	99
D-4	May 17th Mean Wave Direction	100
D-5	July 27th Height Spectra	102
D-6	July 27th Mean Wave Direction	103
E-1	3DM to Kearfott Accelerometer Comparison	106
E-2	3DM to Kearfott Angular Rate Comparison	107
E-3	3DM to Kearfott Euler Angle Comparison	108
E-4	3DM to Kearfott Vehicle Velocity Comparison	109
E-5	Bottom Track to Kearfott Vehicle Velocity Comparison	110
F-1	3DM X-Accelerometer and Roll Rate Gyro Noise Spectrum	114
F-2	3DM Pitch and Integrated Gyro Noise Spectrum	115
F-3	3DM Roll and Integrated Gyro Noise Spectrum	115

List of Tables

3.1	MVCO ADCP Settings	35
3.2	REMUS 100 Specifications	36
3.3	REMUS DVL Settings	37
3.4	Microstrain Configuration Settings	38
3.5	Datawell HF Transmitter Specifications	41
3.6	Mission Information and Conditions	45
6.1	Platform and Recommended Sensors for Accurate Wave Analysis	74

Chapter 1

Introduction

1.1 Motivation

Currently accepted methods for measuring ocean waves are limited to stationary bottom mounted triplet devices, Acoustic Doppler Current Profilers (ADCP), and arrays of pressure sensors, as well as moored buoys. While these methods have been proven to be effective at measuring ocean waves at a given location (Strong et al., 2000; Jeans et al., 2003), they are limited in that they are unable to provide accurate wave information to systems that move out of their immediate sensing area, for example an Autonomous Underwater Vehicle (AUV) or submarine.

Surface wave information can be vital to AUV operations, primarily due to the large hydrodynamic effects of surface waves on AUV station keeping (Riedel and Healey, 1998). Accurate knowledge of surface wave characteristics at the location of the AUV provides input for the AUV's control systems, and allows for better submerged control and operation.

Similar effects can be seen in the case of larger underwater platforms such as naval submarines. Little information is known to the crew about the current sea state while the vessel is submerged. Sea state estimated by passive sonar, or previous observations, does not provide the necessary understanding of the current sea surface activity. This can lead to challenging depth keeping scenarios at periscope depth, which can result in broaching of the submarine and possible counter detection, not

to mention the increased risk of collision due to the loss of depth control. Accurate information regarding the surface ocean wave height and direction would lead to better course and speed selections prior to ascent and allow for safer ship operations while at periscope depth.

1.2 Objectives

The primary objective of this research is to develop the capability to measure the height and direction of ocean surface waves remotely from an underwater vehicle. The main problem in doing this is measuring the wave-correlated motion of the AUV and removing it. By combining measurements from upward- and downward-looking Doppler sonars, such as the ADCPs that are standard on REMUS-class AUVs or, in the case of submarines, an upward looking ADCP and the shipboard Inertial Navigation System (INS), I intend to prove the ability to measure the surface wave directional spectrum and non-directional surface height spectrum and thus infer the surface wave mean direction and amplitude.

To verify the results of this research, the data from a moving REMUS ADCP is compared both to a Datawell Directional Waverider buoy, and a bottom mounted upward looking ADCP located at the 12 meter node at the Martha's Vineyard Coastal Observatory (MVCO). The combined data from the wave buoy, and the fixed and moving ADCPs, allow investigation of the following issues that directly affect the quality of the inferred wave height and direction:

[1] How well can the wave-induced motion of the AUV be measured and removed from the data? We show that when operating in shallow water, the vehicle velocity relative to the bottom measured using the downward-looking ADCP is sufficient to remove the wave-correlated vehicle motion from the velocities measured by the upward-looking ADCP. However, in deeper water another means of accomplishing this is required. Our REMUS carried a high accuracy Kearfott Inertial Navigation Unit (INU) which measures the vehicle attitude and heading as well as its translational velocity. We demonstrate that the Kearfott measurements are also sufficient

to correct the ADCP water-mass velocities and estimate wave velocities in an earth-referenced frame.

[2] What system configurations and environments allow for the most accurate estimation of wave height and direction? Most REMUS vehicles have upward and downward looking ADCPs. However, because of its cost, few are equipped with the Kearfott INU. Because of this, we also investigated the feasibility of using a Microstrain 3DM-GX3-25 Attitude Heading Reference System (AHRS) to measure the vehicle attitude and velocity. This is an inexpensive, off-the-shelf, sensor based on MEMS technology. We show that, with care, this AHRS also has acceptable performance for estimating the vehicle motion and can be used in place of the Kearfott INU.

[3] How do we compensate for the Doppler shift induced by the translational speed of the AUV? The forward motion of the AUV induces a Doppler shift in the apparent wave frequency that depends on the angle between the vehicle velocity and the waves. We apply conventional “triplet” processing techniques to the earth-referenced wave orbital velocities in order to estimate the mean wave direction as a function of apparent frequency. Since the Doppler shift is relatively small and the variation of wave direction with frequency is slow, this estimate of wave direction can be used to solve the dispersion relation for the intrinsic wave frequency.

1.3 History of Ocean Wave Spectral Analysis

The random nature of the ocean surface was first addressed by the work of Barber and Ursell (1948). Fueled by results of Rice (1944) on the statistics of random noise, they performed spectral analysis on wave records obtained from bottom-mounted pressure sensors. The statistical distributions of waves and random surfaces were later described by Longuet-Higgins (1952, 1957).

The ability to determine the frequency and directional spectrum directly from sensor measurements came about in the early 1960’s using pitch and roll buoys (Longuet-Higgins et al., 1963) and pressure sensor-current meter (PUV) combinations (Nagata,

1964). These are considered point sensors as they determine the spectrum of wave components measured at a single point in the wave field.

The earliest use of Doppler sonar to measure ocean gravity waves inferred the spectrum from measurements of the surface wave orbital velocities using horizontally-projected (Pinkel and Smith, 1987; Krogstad et al., 1988) or vertically-fanned beams (Smith, 1989; Trevorrow and Booth, 1995). However, these early demonstrations used specialized sonars, and there was an obvious incentive to extend the use of bottom-mounted, upward-looking ADCPs to also measure waves in addition to current profiles (Terray et al., 1990, 1997; Strong et al., 2000).

1.4 Recent AUV Wave Research Efforts

Wood et al. (2005) attempted to measure waves using a subsurface ADCP moored in 1400 meters of water south of Australia. Earth-referenced velocities were estimated using a second downward-looking ADCP mounted in tandem with the upward-looking unit. The latter ADCP measured velocities below the wave layer, and wave-coherent velocities at depth were attributed to the wave-induced motion of the mooring and used to correct the velocities measured by the upward-looking ADCP.

Riedel and Healey (2005) presented wave direction measurements obtained from the Naval Postgraduate School’s “Phoenix” AUV using a Sontek ADV three-axis point velocity sensor. More recently, Goodman et al. (2010) published wave height (but not direction) measurements from a REMUS-100 using the measured pressure and vertical acceleration of the vehicle.

However none of these efforts included comparison wave measurements from other sensors, such as a buoy. Therefore, the ability to successfully measure wave height and direction remotely from a moving AUV has not yet been demonstrated.

1.5 Overview of Study

This thesis is organized as follows:

Chapter 2 describes the ADCP, its history, and fundamental concepts behind its operation. It discusses methods used to analyze ADCP data and describes the mathematical approach to developing surface wave height and directional spectra. Additionally, the process of assessing the inherent error in the mean wave direction is provided.

Chapter 3 goes into detail about the experiments conducted to obtain the data analyzed for this research. The sensors employed are discussed, including their basic configuration settings and the type of information drawn from each sensor. Some background information is given regarding the logistics of the missions, and the general details of each mission is discussed.

Chapter 4 discusses the various pre- and post-processing routines used to analyze the data from the deployed sensors. Specifics regarding sensor data types, sensor signal correlation, and data sampling is presented. Example spectra developed from each sensor or combination of sensors is presented.

Chapter 5 compares the outputs of the individual sensors to determine which sensors allow for the best results. Height and directional spectra are developed and compared from each sensor and compared to the wave buoy spectra to determine accuracy.

Chapter 6 develops the conclusions of the research based on the results presented in the previous chapters. It describes multiple vehicle configurations and outlines their ideal environment for obtaining accurate wave information. Further research is discussed and final recommendations for usage in the field are outlined.

Various technical details are discussed in the Appendices.

Chapter 2

Acoustic Doppler Current Profiler

2.1 Introduction

The Acoustic Doppler Current Profiler (ADCP) is an active sonar system that is able to measure the 3-dimensional components of water velocity at regular depth intervals in the water column. ADCPs are a proven technology for measuring currents. More recently fixed ADCPs have been demonstrated to be able to provide accurate surface and directional spectra of ocean waves (Terray et al., 1990, 1997).

ADCPs are currently developed by a number of companies. Nortek, Sontek, and Teledyne–RDI are the current leaders in the industry and each have been responsible for different innovations in the research and development of ADCPs. While the theory behind the operation of the ADCP is similar for the three manufacturers, the processing described in this chapter applies specifically to the RDI Sentinel four-beam ADCP.

2.2 ADCP History

The first ADCP was developed in 1979 and was based on a standard Doppler navigator system originally developed to measure the speed of ships (Rowe and Young, 1979). Initially created as a narrowband system that utilized single pulse incoherent Doppler processing techniques, the technology has evolved to using broadband pulse-to-pulse

coherent processing that has led to higher accuracy velocity measurements and finer depth resolution (Rowe et al., 1986; Brumley et al., 1991).

2.3 Theory of Operation

The following is a brief discussion on the theory behind the operation of the ADCP. A more detailed discussion of the principles of the ADCP can be found in the RDI Acoustic Doppler Current Profiler - Principles of Operation (Gordon, 2011).

2.3.1 The Doppler Effect

An ADCP transmits pulses of acoustic energy that are backscattered from small particles and plankton suspended in the water. These scatterers are assumed to be moving with the same velocity as the water. The reflected sound is Doppler-shifted in proportion to the relative velocity between the particle and the transducer face. The received Doppler shifted frequency is given by

$$F_d = 2F_s(V/C) \tag{2.1}$$

where F_d is the Doppler shifted return frequency, F_s is the known transmit frequency, V is the relative velocity between the scatterer and the transducer, and C is the speed at which sound travels in the medium. The full derivation of (2.1) can be found in Appendix A.

2.3.2 Range Gating

The Teledyne-RDI ADCP has four beams at 90° azimuthal increments, inclined at a 20° angle with respect to the normal from the transducer housing. It measures the component of velocity along each beam, and is able to develop a velocity profile of the water column by range gating the backscattered return signal. This is based on the fact that returns from particles farther away take longer to get back to the

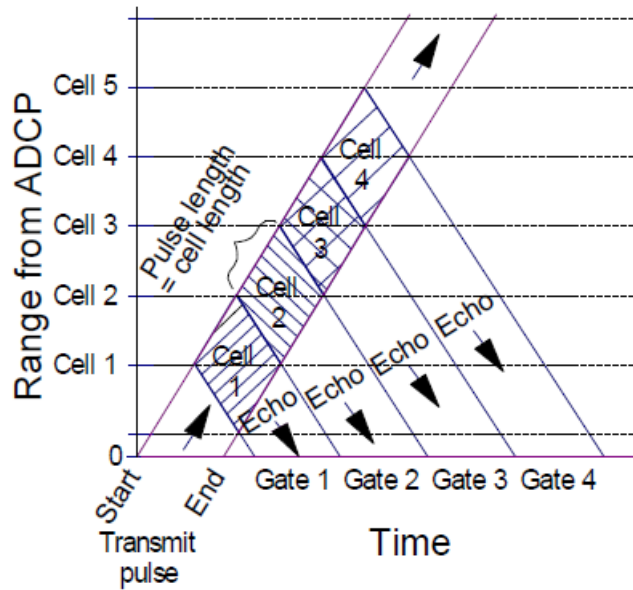


Figure 2-1: The time it takes for the scattered ping to return to the ADCP is dependent upon the range at which the ping is scattered from the transducer. By processing the return echo in incremental gates, the ADCP is able to develop a depth-velocity profile. Graphic from Gordon (2011) Chapter 5.

transducer, so that there is a direct translation between the reception time of the echo and range to the scattering event.

Figure 2-1 shows how the transmitted ADCP pulse and echoes travel through space.

2.3.3 ADCP Coordinate Frame

The ADCP measures the component of water velocity projected along each beam at a number of ranges along the beam. This creates a sparse spatial array of velocity observations. In the case of the bottom mounted ADCP, this collection of velocities can be inverted, using array-processing techniques, to give an estimate of the wave frequency–direction spectrum. However, because the ADCP is installed on an AUV that is moving in a wave–correlated way, the location of the ADCP range bins in space is changing on the same time scale as the waves, preventing us from using the same array-processing techniques used in the static, bottom mounted case.

Instead, based on the fact that the AUV is operating relatively close to the surface, the lateral separation between range cells along the various beams is much less than the wavelength of the dominant waves. Because of this approximation, we can combine velocities along the four beams to estimate the three components of wave velocity in the same way as is done conventionally for currents.

This requires that we first combine the along-beam velocities to approximate the vector velocity in the AUV instrument frame. This velocity is then transformed into a fixed, earth-referenced, coordinate frame using the attitude and heading measured by the inertial sensors on the vehicle. The transformation from beam to instrument coordinates is performed by the matrix equation (2.2)

$$\begin{bmatrix} X \\ Y \\ Z \\ e \end{bmatrix} = \begin{bmatrix} a(b_1 - b_2) \\ a(b_4 - b_3) \\ b(b_1 + b_2 + b_3 + b_4) \\ d(b_1 + b_2 - b_3 - b_4) \end{bmatrix} \quad (2.2)$$

X , Y , and Z are the instrument frame coordinates shown in Figure 2-2, e is the error velocity, and b_1 , b_2 , b_3 , and b_4 are the measured beam velocities. a , b , and d are coefficients based on the geometry of the beam configuration. $\alpha = 20^\circ$ represents the beam angle from the transducer face to the vertical axis for both the RDI Sentinel and REMUS ADCPs.

$$a = \frac{1}{2 \sin(\alpha)} = 1.4619 \quad b = \frac{1}{4 \cos(\alpha)} = 0.2660 \quad d = \frac{a}{\sqrt{\alpha}} = 1.0337$$

Once beam velocities have been transformed into instrument coordinates, they can be rotated into the earth's fixed coordinate system using the ADCP's on-board heading and tilt sensors or a separate attitude sensor. The following rotation matrix is used to rotate the velocities from the instrument coordinate frame to the fixed,

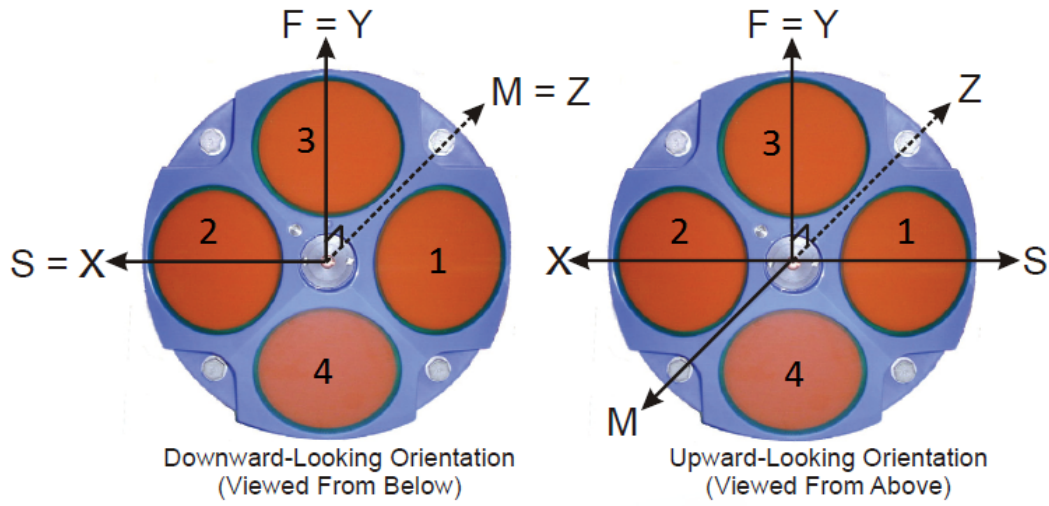


Figure 2-2: ADCP Downward and Upward Instrument Frame Coordinate System. Graphic from Tel (2008) Chapter 5.5.

earth-referenced frame.

$$M = \begin{bmatrix} CH & SH & 0 \\ -SH & CH & 0 \\ 0 & 0 & 1 \end{bmatrix} \begin{bmatrix} 1 & 0 & 0 \\ 0 & CP & -SP \\ 0 & SP & CP \end{bmatrix} \begin{bmatrix} CR & 0 & SR \\ 0 & 1 & 0 \\ -SR & 0 & CR \end{bmatrix} \quad (2.3)$$

$$\begin{bmatrix} N \\ E \\ U \end{bmatrix} = M \begin{bmatrix} X \\ Y \\ Z \end{bmatrix} \quad (2.4)$$

N , E , and U are the North, East, and Up component velocities in the earth coordinate system. The above rotation matrix, and the beam-to-instrument conversions, are given in the RDI Coordinate Transformation Handbook (Tel, 2008).

2.4 ADCP Wave Analysis

One of the primary objectives of this research is to compare various ways of sensing and removing the wave-correlated vehicle motion in order to produce accurate height

and directional wave estimates. We validate the various approaches by how well they give the non-directional height spectrum and the mean wave direction at each frequency based on UVW processing of the ADCP velocities. The relevant expressions are derived from linear random wave theory and spectral analysis. The following sections highlight the key ideas and equations used to develop the height and mean wave direction estimates used in later chapters. A full derivation of the equations used can be found in Appendix B and C.

2.4.1 Linear Wave Theory

Linear wave theory provides the basis for understanding how surface waves propagate. Starting with a wave that travels in a two dimensional plane, the general form for the displacement on the free surface of the fluid is given by

$$\eta(\mathbf{x}, t) = a \sin(\mathbf{kx} - \omega t) \quad (2.5)$$

Solving Laplace's equation, the expression for the velocity potential is given by

$$\varphi(x, z, t) = \frac{a\omega}{k} F(kz) \sin(kx - \omega t) \quad (2.6)$$

where $F(kz)$ is the vertical structure function given by

$$F(kz) = \frac{e^{k(2H+z)} + e^{-kz}}{e^{2kH} - 1} = \frac{\cosh(k(z + H))}{\sinh(kH)} \quad (2.7)$$

The dispersion relation which describes how angular frequency and wave number are linked is given by

$$\omega^2 = gk \tanh(kH) \quad (2.8)$$

The dispersion relation, vertical structure function, and velocity potential are key elements used in linear wave theory and are the primary components used to develop the wave height spectrum and the mean wave direction estimates. The full derivation of each of these is given in Appendix B.

2.4.2 Surface Spectrum Analysis

The method we use to estimate the height spectrum and mean wave direction from the velocities measured by the upward-looking ADCP on the REMUS is the same method applied to “triplet” or “point” sensors. However, whereas “point” sensors measure the waves at a single point in the wave field, the ADCP measures a mix of velocity components at many points, and therefore we combine the beam velocities as discussed above to approximate “point” measurements at various ranges from the instrument.

The error in this approximation depends on kd , where $d = Z \tan \alpha$ is the separation between a range cell at a distance Z above the instrument and the center line of the beams, and $k = 2\pi/\lambda$ is the wavenumber of the wave. The experiments reported here were carried out in water depths of around 15 m, and the frequency of the energy-containing waves in the spectrum was roughly 0.125 Hz. We use velocities at a typical vertical distance of ~ 2 m, so that $kd \sim 0.06$. The leading corrections to this are of order $(kd)^2 \sim 0.004$, and so are negligible for the REMUS data (E. Terray, *personal communication*).

“Point” sensors generally measure three wave dependent quantities, two of which are dependent on direction while the third is not. In our case, the ADCP measures the two horizontal components of velocity, which are directional, and the vertical velocity, which is non-directional. By cross-correlating these velocities with each other, the wave height and the first four complex Fourier coefficients of the directional spectrum can be inferred.

2.4.3 Wave Height Analysis

The MVCO ADCP is configured to report individual measured beam velocities. The non-directional surface height spectrum S_η can be calculated from the sum of the individual beam velocities and is given by

$$S_\eta = \frac{S_{u_1} + S_{u_2} + S_{v_1} + S_{v_2}}{2\omega^2(F(kz)^2 \sin^2 \alpha + 2F'(kz)^2 \cos^2 \alpha)} \quad (2.9)$$

where $S_{u_1}, S_{u_2}, S_{v_1}$, and S_{v_2} are the four beam auto-spectra, ω is the angular frequency, $F(kz)$ is the vertical structure function, and α is 20 degrees for RDI ADCPs.

The REMUS ADCP reports water velocities already rotated into instrument coordinates. The wave height spectrum from the REMUS ADCP is then calculated by

$$S_\eta = \frac{S_w}{\omega^2 F'(kz)^2} = \frac{S_u + S_v}{\omega^2 F(kz)^2} \quad (2.10)$$

where S_u, S_v, S_w are the instrument coordinate velocity auto-spectra, ω is the angular frequency, $F(kz)$ is the vertical structure function.

The significant wave height is defined as 4 times the standard deviation of the surface displacement and is given by

$$H_s = 4\sqrt{\int S_\eta df} \quad (2.11)$$

2.4.4 Wave Direction Analysis

The directional coefficients, c_n are defined as the Fourier coefficients in the expansion of the frequency-direction spectrum, $D(\omega, \theta)$

$$D(\omega, \theta) = \frac{1}{2\pi} \sum_{n=-\infty}^{+\infty} c_n(\omega) \exp(-in\theta) \quad (2.12)$$

where $\omega = 2\pi f$ is the angular frequency. Inverting this relation gives

$$c_n(\omega) = \int_{-\pi}^{+\pi} d\theta D(\omega, \theta) \exp(in\theta) \quad (2.13)$$

The directional coefficients are complex, and it is conventional to write c_n in terms of its real and imaginary parts as

$$c_n = a_n + ib_n \quad (2.14)$$

so that

$$a_n = \overline{\cos(n\theta)} \quad \text{and} \quad b_n = \overline{\sin(n\theta)} \quad (2.15)$$

The quantities a_1 and b_1 give an estimate of the mean wave direction at each frequency as

$$\bar{\theta} = \text{atan2}(b_1, a_1) = \text{angle}(c_1) \quad (2.16)$$

The first four directional coefficients are directly estimated by the spectra and cross-spectra of the beam velocities and are given by

$$a_1 = \frac{Q_{wu}}{\sqrt{S_w(S_u + S_v)}} \quad (2.17)$$

$$b_1 = \frac{Q_{wv}}{\sqrt{S_w(S_u + S_v)}} \quad (2.18)$$

$$a_2 = \frac{S_u - S_v}{S_u + S_v} \quad (2.19)$$

$$b_2 = \frac{2S_{uv}}{S_u + S_v} \quad (2.20)$$

2.4.5 Error in the Mean Direction Estimate

The height and direction estimates above are subject to bias and random error.

Bias: There are several sources of bias, but the main ones are due to rotational errors. However, the bias is second order in tilt. This can be seen by the following example: Suppose the instrument is tilted in the u - w plane by an angle β . Then the measured u and w velocities (denoted by primes) are

$$u' = u \cos \beta - w \sin \beta \quad (2.21)$$

$$w' = u \sin \beta + w \cos \beta \quad (2.22)$$

Therefore

$$S_{w'} = S_w \cos^2 \beta + S_u \sin^2 \beta \quad (2.23)$$

$$R_{u'w'} = C_{u'w'} + iQ_{u'w'} = -(S_w - S_u) \sin 2\beta + iQ_{uw} \cos 2\beta \quad (2.24)$$

Assuming that β is small, we see that the bias in S_w is $\mathcal{O}(\beta^2)$, as is the bias in Q_{uw} . Therefore, the biases in the mean wave direction are second order. Since the

tilts observed in the AUV data were small (typically less than $5 - 6^\circ \sim 0.1$ radians, the error is of order a few percent, and hence can be neglected.

Random Error: The mean wave direction is estimated from the directional coefficients using (2.16).

Long (1980) shows that the variance of the estimate of the mean wave direction due to the statistical uncertainty in estimating the various spectra and cross-spectra required is given by

$$\text{var}(\bar{\theta}) = \frac{(a_1^2 + b_1^2) - (a_1^2 - b_1^2)a_2 - 2a_1b_1b_2}{2\nu(a_1^2 + b_1^2)^2} \quad (2.25)$$

where ν denotes the degrees of freedom in the spectral estimates used to estimate the coefficients a_1, b_1, a_2 , and b_2 .

The square root of (2.25) is the standard deviation of the mean wave direction as a function of frequency. We use \pm one standard deviation as an error bar on our estimate of the mean wave direction at each frequency.

Chapter 3

Experiment

3.1 Introduction

Measuring ocean waves from a moving platform first requires a moving platform. We used a REMUS-100 AUV operated by the Oceanographic Systems Laboratory in the Department of Applied Ocean Physics and Engineering at the Woods Hole Oceanographic Institution (WHOI). This vehicle was chosen because, in addition to upward- and downward-looking ADCPs, it also carries a high accuracy Kearfott Inertial Navigation Unit (INU). A low cost Microstrain 3DM-GX3-25 Attitude-Heading-Reference-System (AHRS) also was integrated into the vehicle to test its capabilities as a lower cost alternative to the Kearfott sensor.

Vehicle operations were conducted around the subsurface node of WHOI's Martha's Vineyard Coastal Observatory (MVCO). The node has a bottom-mounted, upward-looking, 1200 kHz ADCP at a depth of 12 m which samples velocities over the full water column at 2 Hz with 0.5 m vertical resolution. Single ping ensembles are available through the MVCO web site. In addition, we moored a Datawell MK-III Directional Waverider nearby. This buoy is commonly-accepted as the "gold standard" for measuring waves in coastal waters (Mettlach and Teng, 2010).

These two sources provide independent, reliable, and accurate wave information. Research has shown that specific surface statistics such as significant wave height and period produced by Datawell directional Waverider Buoys and RD Instrument

ADCPs agree well (Jeans et al., 2003), although thorough comparisons of the wave spectra generated by these two instruments have not been published. Combined, the Directional Waverider and ADCP provide the most accurate means of testing the results from the moving REMUS ADCP data.

3.2 Funding

Funding for this experiment was provided by WHOI’s “Access to the Sea” program, which provides funds for research opportunities that promote WHOI’s ongoing commitment to ocean research and development.

3.3 Equipment and Sensors

The following sections give a basic description of the operation and initial configuration of each of the sensors employed during this experiment. Special functions of the equipment are outlined, and a brief discussion on the initial setup and data output of each sensor is covered.

3.3.1 Martha’s Vineyard Coastal Observatory

Martha’s Vineyard Coastal Observatory was established in 2001 and consists of multiple stations that measure and record data to help scientists gain a better understanding of coastal processes. Stations include a lab at the Katama Airpark, an undersea node at 12 m depth equipped with an ADCP and conductivity, temperature, and depth (CTD) sensor, and an air-sea interaction tower (ASIT) equipped with various sensors.

ADCP

The MVCO uses an RDI Sentinel 1200 kHz ADCP. It is located at 41 20.1950’ N, 70 33.3865’ W. Its operation is discussed in detail in Chapter 2.

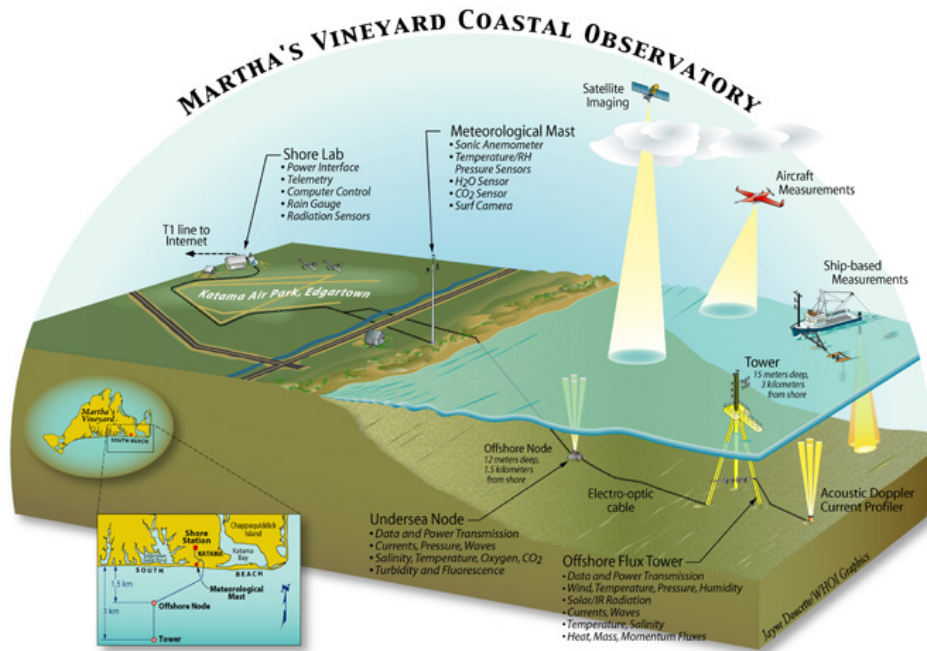


Figure 3-1: Martha's Vineyard Coastal Observatory. Graphic from Doucette (2010).

Table 3.1: MVCO ADCP Settings

Command	Value	Description
WP	1	Number of pings per ensemble
EX	00000000	Beam Coordinates, No Tilts, No 3-Beam Solutions
WS	50	Bin size (cm)
WN	25	Number of bins
ES	32	Salinity

3.3.2 REMUS-100

The Remote Environmental Monitoring Units (REMUS) are operated by the WHOI Oceanographic Systems Lab (OSL). OSL is responsible for developing and maintaining the most advanced AUVs available today.

The REMUS-100 vehicle was chosen for this experiment due to its ease of use, low number of required operators, and standard sensor package load-out. The vehicle comes equipped with a high accuracy Kearfott INU and upward and downward looking ADCPs.



Figure 3-2: REMUS-100 vehicle strapped to the deck of the R/V *Tioga* prior to deployment on April 26th.

Table 3.2: REMUS 100 Specifications

Vehicle Diameter	19 cm
Vehicle Length	160 cm
Weight in air	38.5 kg
Max Operating Depth	100 m
Endurance	8-10 hours
Propulsion	Direct drive brushless motor to open 3-bladed propeller
Velocity range	Up to 4.5 knots
Navigation	Long baseline; Doppler assisted dead reckoning; INS; GPS
Tracking	Emergency transponder, mission abort, and in mission tracking

ADCP

The ADCPs installed on REMUS vehicles are primarily used for submerged acoustic navigation. Specifically, REMUS vehicles are equipped with RDI's Workhorse Navigator Doppler Velocity Log (DVL) system. The general operation of the DVL is identical to the ADCP discussed in Chapter 2. The primary use of the downward looking beams on the DVL are for bottom tracking to allow for better submerged navigation and tracking.

The DVL system provides accurate water current information (Fong and Jones, 2006). Because the DVL is attached to a moving AUV, there are biases in the water velocities in the direction of motion. (Fong and Monismith, 2004) We attempt to remove these biases using the high accuracy Kearfott INU, ADCP bottom track, and

Microstrain 3DM-GX3-25.

Table 3.3: REMUS DVL Settings

Command	Value	Description
WP	1	Number of pings per ensemble
EX	10111	Ship mode, use tilts, 3 beam solutions
WS	25	Bin size (cm)
WN	20	Number of bins
BP	47	Bottom pings per ensemble
WV	250	Ambiguity velocity
ES	31	Salinity

Kearfott

The T-16 Kearfott INU installed on REMUS vehicles uses an advanced monolithic ring laser gyro system. In conjunction with the REMUS DVL, it is able to provide precise inertial measurements that further aid the REMUS in underwater navigation. Typical error accumulations of less than 10 meters per hour have been seen in REMUS 6000 deployments (Sharp and White, 2008).

Microstrain 3DM-GX3-25

The Microstrain 3DM-GX3-25 is a small attitude heading reference system. It is a Microelectromechanical systems (MEMS) device that contains a tri-axial accelerometer, gyro, and magnetometer. The 3DM-GX3-25 was integrated directly into the REMUS-100 vehicle, allowing for data to be polled and stored directly by the REMUS logging system.

Since the Kearfott INU discussed above is expensive and not standard on all REMUS vehicles, it was decided that a small inexpensive alternative be tested to determine if similar corrections could be made to the ADCP water velocity measurements and still yield acceptable wave measurements.

The 3DM-GX3-25 is able to output various inertial measurements such as accelerations, attitude, and angular rates. During the first three missions, the instrument was set to continuously stream raw acceleration, angular rate and magnetometer data at



Figure 3-3: The 3DM-GX3-25 Attitude Heading Reference System.

50Hz, and poll for heading, attitude, delta velocity, and angular rate vectors at 4.5Hz. Prior to the last mission, the settings were adjusted and the device was set to stream raw acceleration, angular rates, magnetometer readings, and the instrument rotation matrix at 25 Hz. This change was to allow for leveling of the accelerometers at the same rate that they were sampled, rather than downsampling the accelerometers to the euler angle rate prior to leveling, as was previously done.

Table 3.4 lists the configuration settings that are set by the 0xDB serial command used during the last deployment.

Table 3.4: Microstrain Configuration Settings

Parameter	Value
Firmware	1.1.32
Decimation Value	20
Data Conditioning	3
Gyro and Accelerometer Digital Filter Window	32
Magnetometer Digital Filter Window	32
Up Compensation	32
North Compensation	32

3.3.3 Datawell Waverider Buoy

The Datawell MKIII Directional Waverider buoy has a diameter of 90 cm and is equipped with GPS, an HF transmitter, and ARGOS transmitter. Data is processed



Figure 3-4: The Datawell MKIII Directional Waverider Buoy shown here in its shipping crate on the WHOI pier following its 4 month deployment near the MVCO.

and stored internally on a type-1 compact flash card and transmitted via HF and relayed to the Argos satellite system.

The buoy is able to measure the surface height spectrum through the use of a single accelerometer oriented with the vertical axis that is mounted on a gravity-stabilized platform. Because the platform remains horizontal at normal wave frequencies, the accelerometer outputs are able to be integrated twice to determine accurate buoy heave measurements.

The directional spectrum is determined by correlating the horizontal motion of the buoy with the vertical heave of the buoy. Two perpendicular accelerometers are in place to measure the horizontal motion of the buoy. In the event that the buoy is tilted, pitch and roll sensors are used to transform the measured accelerations to horizontal accelerations.

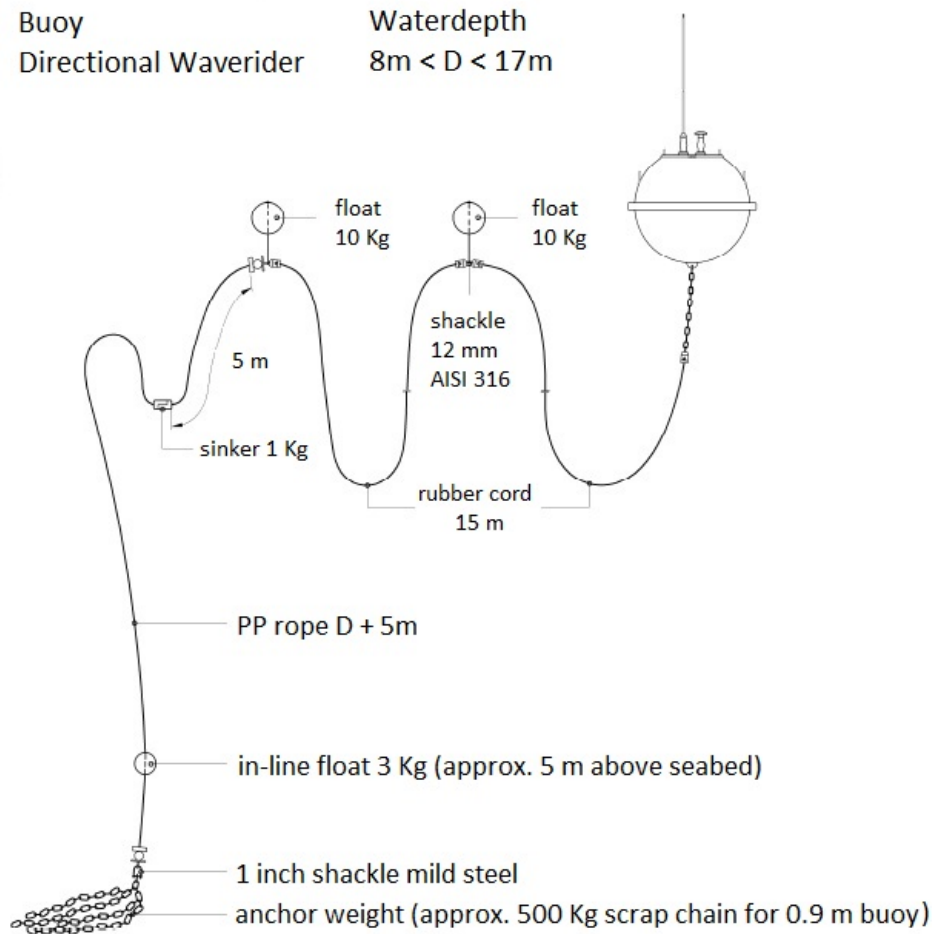


Figure 3-5: This figure shows the mooring configuration for the Datawell MKIII Directional Waverider buoy when the buoy is moored in 8 to 17 meters of water. The entire mooring system was provided by Datawell with the exception of the anchor. A 500 Kg anchor was provided by the WHOI mooring shop. Figure from Dat (2010) Chapter 5.8

Mooring System

Waverider buoys must be free to move with the ocean waves, yet must be moored to prevent the buoy from drifting out to sea. Mooring can inhibit the motion of the buoy, therefore negatively affecting the accurate representation of the ocean surface. Datawell provides a mooring system specifically designed to prevent the corruption of wave information by the mooring. The key components of the system are two 15 meter rubber cords that allow the wave buoy to act as a free floating particle on the surface of the water and follow the wave motion.

HF Transmitter and Receiver

The Datawell MKIII Directional Waverider buoy is equipped with a HF transmitter that serves as the primary method of data transmission to the shore. The generated wave data is received by a Datawell RX-D type 2 HF receiver that interfaces with a PC through a serial port. The data is processed by the Datawell W@ves21 software where a spectral plots can be viewed directly. The receiving antenna and receiver were installed on the roof of Bigelow Laboratory in downtown Woods Hole.

Table 3.5: Datawell HF Transmitter Specifications

Parameter	Specification
Output Power	75 mW
Frequency	29.825 MHz
Bandwidth	± 80 Hz
Transmit Range	50 Km

Argos Satellite System

The Argos system is used primarily as a method for tracking a buoy adrift. It is also able to transmit simple wave information which can be monitored and downloaded from the Argos system website.

Internal Logging

Data generated by the Waverider is processed and stored internally on a type-1 compact flash card. Raw displacements and spectral information files are created every 30 minutes and written to the card. The card can hold up to 36 months of wave information. The Datawell W@ves21 software is able to process the generated files and create height and directional spectra from the raw displacement and spectral files.

3.4 Logistics and Mission Planning

The R/V *Tioga* is an aluminum hulled coastal research vessel owned and operated by the Woods Hole Oceanographic Institute. The *Tioga* was an ideal platform for us to



Figure 3-6: The WHOI Research Vessel *Tioga* shown moored at its home berth at the WHOI pier in Woods Hole, Massachusetts.

deploy the Waverider buoy and conduct REMUS missions due to its high speed and low daily expense. The crew consists of only the Captain and first mate, who both have considerable experience deploying and retrieving equipment at the MVCO.

Safety is always the primary focus for any mission, so planning a trip in seas that would yield effective wave measurements, while still allowing for safe deployment and recovery of the vehicle, was the first priority. The ideal conditions, within the ability of the *Tioga*, were found to be an average wave height of four feet with a period between six and eight seconds.

The following sections describe the deployment mission plans and give a description of sea environment as reported from various MVCO sensors. Table 3.6 lists various parameters from each of the missions. Additional discussion regarding the mission objectives, challenges, and results can be found in Appendix D.

3.4.1 April 20th 2012

The initial deployment was made in calm seas with the primary objective of determining if the bottom mounted MVCO ADCP would interfere with the REMUS ADCP. The REMUS mission consisted of running circles of varying size around the MVCO 12 meter node. Additionally, some north and south legs were run to assess the topography of the area and to obtain some initial measurements for wave analysis. Figure

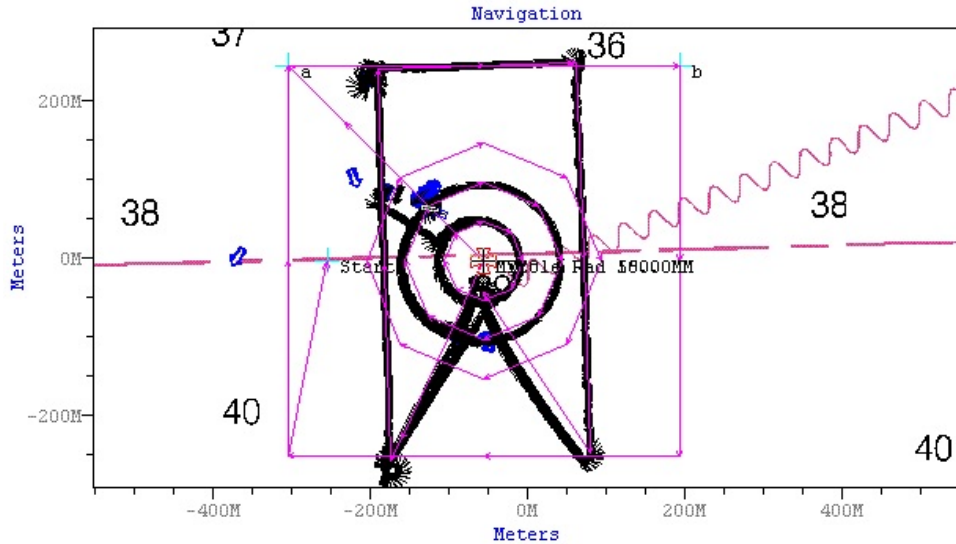


Figure 3-7: REMUS Mission Path April 20th 2012

3-7 shows the general path of the vehicle. While the REMUS ran its mission, the Datawell Waverider buoy was deployed near the MVCO 12 meter node.

Integration of the Microstrain into the REMUS software package was not completed prior to this mission. All other sensors were fully operational.

Initial review of the ADCP data found that there was no noticeable interference between the REMUS and MVCO ADCPs. Future missions were planned without the circular pathing and would focus on north and south legs for wave analysis.

3.4.2 April 26th 2012

The primary objective of this mission was to obtain a data set with all sensors operational. Seas were choppy from the south with a six second period and 3 foot mean height. The software for the Microstrain sensor was completed and bench tested successfully prior to this mission, however post-mission analysis found that the Microstrain had faulty accelerometers and the sensor was removed from the vehicle and returned to the vendor for repairs.

This mission consisted of a rectangular pattern centered around the MVCO node. Legs were driven at two and four meters depth, and the vehicle was programmed to alternate between driving at constant depth and constant altitude. This was done

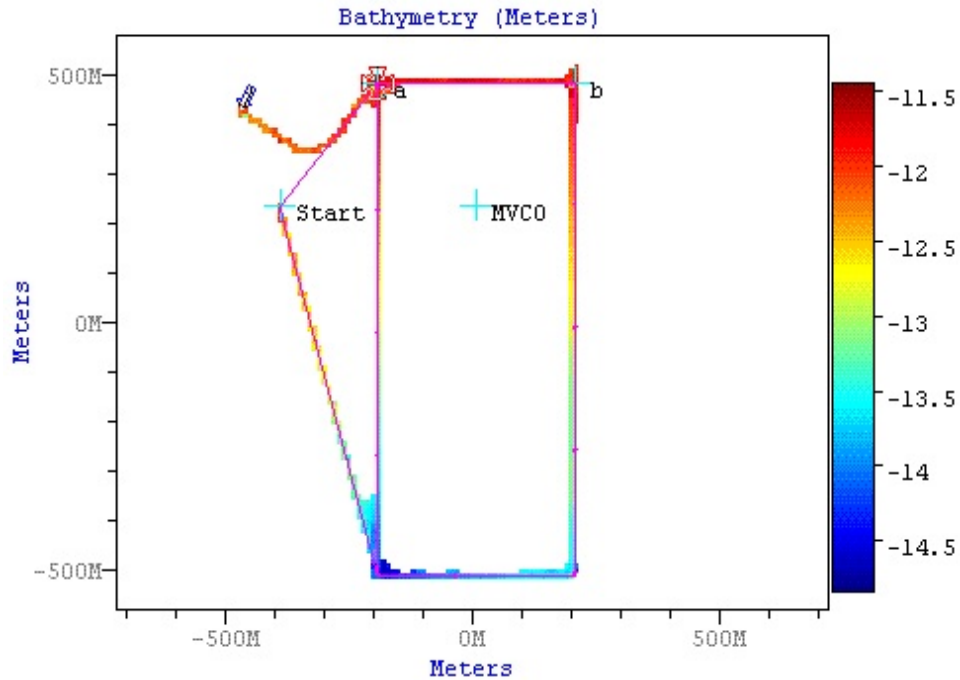


Figure 3-8: REMUS Mission Path and Bathymetry April 26th 2012

to see how the vehicle control system compensated for the waves, as we wanted the vehicle to be as heavily influenced by the wave motion as possible.

Figure 3-8 shows the mission path and bathymetry of the water around the MVC0.

3.4.3 May 17th 2012

The May 17th mission used the same mission plan as the April 26th mission. The 3DM was repaired and was fully operational during this mission. During post-processing however, it was found that the magnetic field generated by the rotating propeller in the stern of the REMUS was biasing the 3DM magnetometers and resulted in unusable heading data. The 3DM was moved to the front of the vehicle for future missions.

The sea conditions for this mission were ideal with average wave height being in the 3-4 ft range.

3.4.4 July 27th 2012

This was the final mission for this research. The 3DM software was updated to allow for additional streaming of the 3DM rotation matrix. This was streamed at the same 25 Hz sample rate as the accelerations and allowed for more accurate leveling of the 3DM accelerometers prior to integration.

Modifications to the mission plan were made in an attempt to obtain the best possible data set. During the second half of the previous mission plan, the vehicle was programmed to maintain constant altitude from the sea floor. Due to the bathymetry of the ocean floor at the mission location, it was decided to instead fly the last half of the mission at constant depth similar to the first half. A 20 meter radius circle was added to the mission path at the beginning of the mission to allow for calibration of the heading data produced by the 3DM.

The weather for the final mission was ideal with a long 4-5 foot swell coming from the south west.

Following the REMUS mission, the wave buoy was recovered and the data was copied from the internal logger and prepared for post-processing. Little action was required for post-processing of the wave buoy data, as all spectral information was calculated on board the buoy and was easily exported to Matlab for plotting.

Table 3.6: Mission Information and Conditions

Parameter	April 20th	April 26th	May 17th	July 27th
Start Time (hh:mm:ss)	12:10:35	11:02:21	10:13:26	14:25:33
Duration (hh:mm:ss)	2:20:49	3:49:31	3:56:36	2:47:36
Distance (NM)	6.03	12.41	12.15	9.4
Vehicle Velocity (Knots)	2.57	3.24	3.22	3.20
Wave Height(m)	0.5	0.7	1.2	1.4
Wave Direction (Degrees From)	165	180	183	210
Wave Period (s)	5	6	7	8
Wind Direction (Degrees From)	200	250	345	240
Wind Speed (m/s)	4.5	2.3	4.8	4.3

Chapter 4

Signal Processing

4.1 Introduction

In order to determine wave direction and height from a moving underwater vehicle, the output of several sensors must be combined. The upward-facing ADCP is the primary sensor used for measuring wave velocity, however, additional subsystems are required to remove the wave-induced motion of the vehicle from the wave velocity record. In this thesis we test three different ways of doing this: [1] subtracting the vehicle's velocity over the bottom as measured by the downward-facing ADCP, [2] subtracting the AUV's inertial velocity as reported by the Kearfott INU, and [3] integrating the acceleration measured by the Microstrain AHRS to compute vehicle velocity and subtracting that estimate from the relative water velocity measured by the upward-facing ADCP. These are then used to estimate the non-directional wave height spectrum and the mean wave direction at each frequency. These two quantities are then compared to their estimates obtained from the Datawell Directional Waverider in order to assess the performance of each of the three methods outlined above.

One complication is that each of the four sensors (up- and down-ADCPs, Kearfott INU and Microstrain AHRS) are independent and sample at times determined by their own internal free-running clocks. Therefore observations common to various pairs of the instruments must be used to synchronize their data streams.

In the following sections we outline in more detail the methodology we followed to process the data and determine the wave height spectrum and mean wave direction.

4.2 Correlation of Sensors

Although all of the sensors produced data at their own rates, they were all recorded by the REMUS data logger. These packets are time-stamped with the logger time. However, since the various instruments were streaming data continuously, the noted time of reception only synchronizes the data to within one sample interval of the logger. This was fine-tuned using cross-correlation analysis between pairs of sensors sharing a common data item. When the two signals are in sync, the resulting cross-correlation plot has a strong peak at or near zero lag. When out of sync, the peak shifts left or right of zero indicating the number of lags or samples by which the signals are out of sync. Interpolation of the location of the cross-correlation peak can be used to resolve the time shift to a fraction of a sample interval.

4.2.1 3DM and Kearfott Correlation

The 3DM and Kearfott are both inertial sensors that measure many of the same properties such as heading, acceleration, and angular rate. Cross-correlating any of these signals from both sensors allows us to determine how well the sensors are in sync.

Figure 4-1 show the cross-correlation between the 3DM and Kearfott accelerometer measurements. A slight delay of only two samples exists between the Kearfott and Microstrain sensors. This is corrected in all data channels during post-processing.

4.2.2 ADCP and Kearfott Correlation

Bottom track data measured by the downward looking ADCP can be compared to the three dimensional velocity data measured by the Kearfott in order to determine the synchronization between the Kearfott and the ADCP data streams.

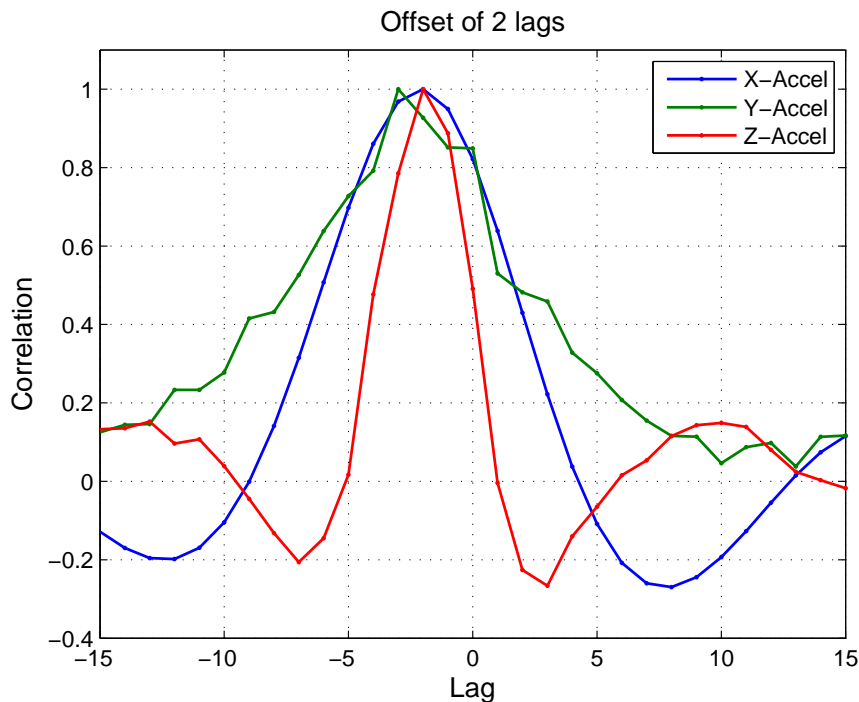


Figure 4-1: Cross-correlation between the Kearfott and Microstrain accelerometers show they are closely in sync.

Figure 4-2 shows an offset of only two samples between all of the bottom track and Kearfott velocity channels. This offset is removed during post-processing.

4.3 REMUS ADCP

The REMUS-100 we used has upward- and downward-looking 1200 kHz ADCPs combined into a single unit. The two ADCPs alternately sample the water column above and below the vehicle. The instrument was programmed to include a bottom-track ping with each velocity profile. The upward and downward ADCP records are combined into a single file and recorded by the REMUS data logger. The REMUS logger also inserts the most recent Kearfott attitude measurements into the ADCP data record whenever one is received. Although the upward- and downward-looking ADCPs were triggered alternately, each data packet contains the time from the ADCP internal clock, thus establishing the time between the Kearfott and water velocity measurements.

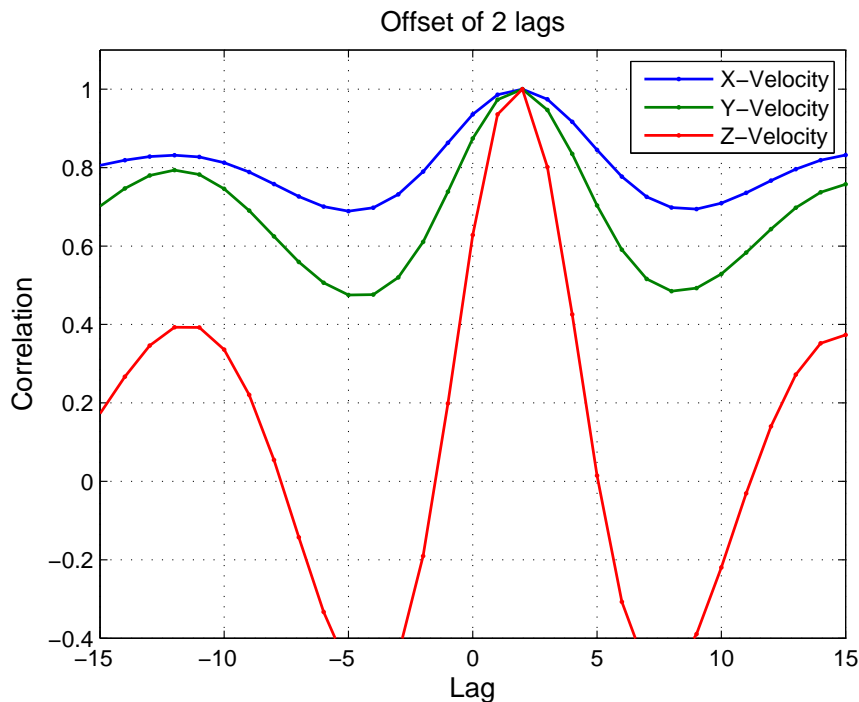


Figure 4-2: Cross-correlation between the ADCP bottom track and Kearfott velocities show a minimal lag.

REMUS ADCP data files are saved in the standard PD0 format developed by RDI, but an additional step is first required to separate the upward and downward looking records into separate files. Each of these is then unpacked into Matlab using the standard ADCP data unpacker. All ADCP signal analysis presented here is done in Matlab.

4.3.1 REMUS ADCP Processing Method

ADCP data from the REMUS is first screened for low ping-to-ping correlation and bad data is removed by linear interpolation.

Once bad data is screened, the ADCP water velocity measurements are corrected by the various inertial sensors or the bottom track velocity measured by the ADCP. Since the bottom track is measured by the ADCP itself, it allows for water velocity corrections without the need for additional sensors. The limitation is that bottom track velocities require the vehicle to be within range of ocean floor, preventing the

ability to measure waves in deep water. The bottom track range is about twice the range of the water velocity measurements, or roughly 60 meters from the vehicle to the ocean bottom when using a 1200 kHz ADCP. ADCP velocities in the vehicle frame still need to be leveled and referenced to a fixed coordinate frame using either the Kearfott INU or Microstrain AHRS attitude and heading measurements. The “triplet” methods in Chapter 2 are then used to process the wave velocity data. Because the REMUS ADCP is configured to report velocities in instrument coordinates rather than individual beam velocities, the surface spectrum is calculated using (2.10). The mean wave direction is estimated as discussed in Chapter 2.

Figure 4-3 and 4-4 show example height and mean wave direction estimates from the REMUS ADCP with and without velocity corrections. It is clear from Figure 4-3 that corrections are needed to obtain any kind of accurate wave information. This is because the vehicle is moving with the wave orbital motion, and therefore measuring very little relative wave velocity. There is very little wave energy in the wave band of the uncorrected spectrum and the mean wave direction is random. Figure 4-4 shows the spectra using bottom track velocity and Kearfott attitude and heading corrections.

The standard deviation of the mean wave direction, as discussed in section 2.4.5, is shown as a dotted red line around the measured mean direction. The estimated significant wave height shown in the legend is found by integrating the height spectrum as discussed in Chapter 2.4.3. The spectrum is integrated from 0.1 Hz to 0.3 Hz to prevent low and high frequency noise from corrupting the height estimate. This integration is performed on all height spectral estimates to determine significant wave heights.

4.4 Kearfott INU

Kearfott data is logged internally by the REMUS vehicle and is exported to disk as a Matlab file following the mission. The Kearfott data contains vehicle attitude and heading information, angular rates, vehicle velocity and acceleration.

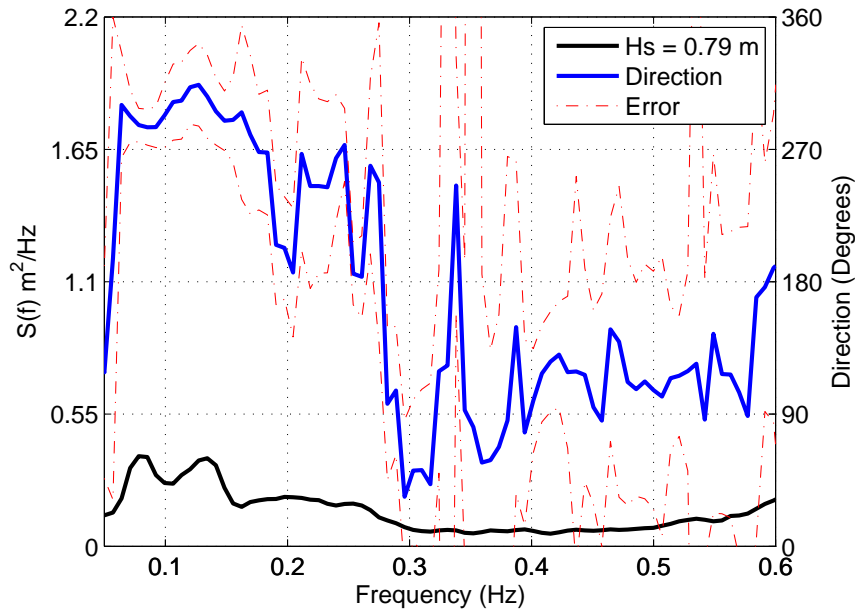


Figure 4-3: This figure shows the REMUS ADCP uncorrected wave height and mean wave direction estimate. There is very little wave energy in the wave band and the mean wave direction is very random with a large error. It is generated from data taken during the July 27th REMUS mission.

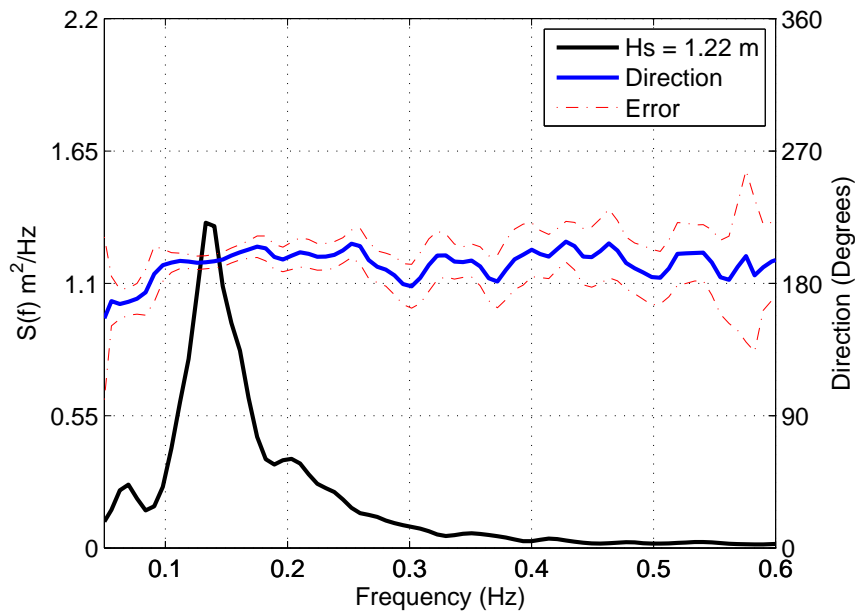


Figure 4-4: This figure shows the REMUS ADCP bottom track corrected wave height and mean wave direction estimate. It is generated from data taken during the July 27th REMUS mission.

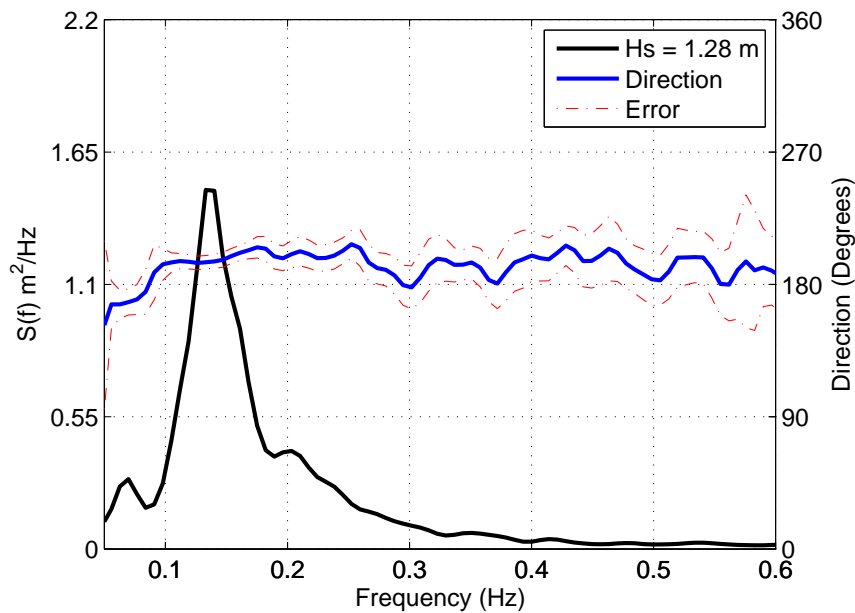


Figure 4-5: This figure shows the REMUS ADCP Kearfott velocity corrected wave height and mean wave direction. It is generated from data taken during the July 27th REMUS mission.

4.4.1 Kearfott Processing Method

The most important variables for wave measurements that are reported from the Kearfott are the pitch, roll, and heading measurements, along with the X, Y, and Z instrument frame velocities. The Kearfott velocities are removed from the measured ADCP velocities to provide stationary referenced wave velocities. Additionally, the heading and attitude values are used to rotate the velocities to the Earth’s coordinate frame to allow for wave direction measurements.

Figure 4-5 shows an example of the height and directional spectrum estimated from the REMUS ADCP using velocity and attitude corrections developed from the Kearfott INU.

4.5 Microstrain 3DM-GX3-25

The 3DM was initially programmed to continuously stream raw accelerometer, magnetometer, and rate gyro data at 50 Hz. Additionally, the REMUS vehicle was

programmed to poll the 3DM for Euler angles and delta velocities and delta angles. Because the REMUS internal clock cycle operates at 9 Hz, the polled data was polled every other cycle resulting in a 4.5 Hz sample rate.

After the May 17th mission, it was decided to change the streamed data to include the vehicle rotation matrix. The vehicle direction cosine matrix gave us the euler angles at the same sample rate as the accelerometers, and therefore permitted us to rotate and integrate the accelerometers without having to downsample. This procedure yielded more accurate vehicle velocities.

Because the streamed data type was significantly larger, the sample rate had to be reduced to 25 Hz to prevent buffer overflow issues with the REMUS data logger, which could result in a loss of data.

4.5.1 3DM Processing Method

Similar to the Kearfott, the primary variables needed from the 3DM are the vehicle velocities, attitude and heading. Although the attitude and heading could be computed directly from the recorded direction cosine matrix, obtaining velocity required that we integrate the reported 3DM accelerations.

Integrating the accelerometers requires first rotating the accelerometer signals from instrument coordinates to earth coordinates. Since integration corresponds (in Fourier space) to dividing by $1/f$, we high-pass filtered the data to avoid amplifying the low frequency sensor noise. After the low frequency components were removed, the leveled acceleration signal was integrated to produce the vehicle earth-referenced velocity components.

Figure 4-6 shows an example of the height and directional spectrum estimated from the REMUS ADCP using velocity and attitude corrections developed from the Microstrain 3DM during the July 27th mission.

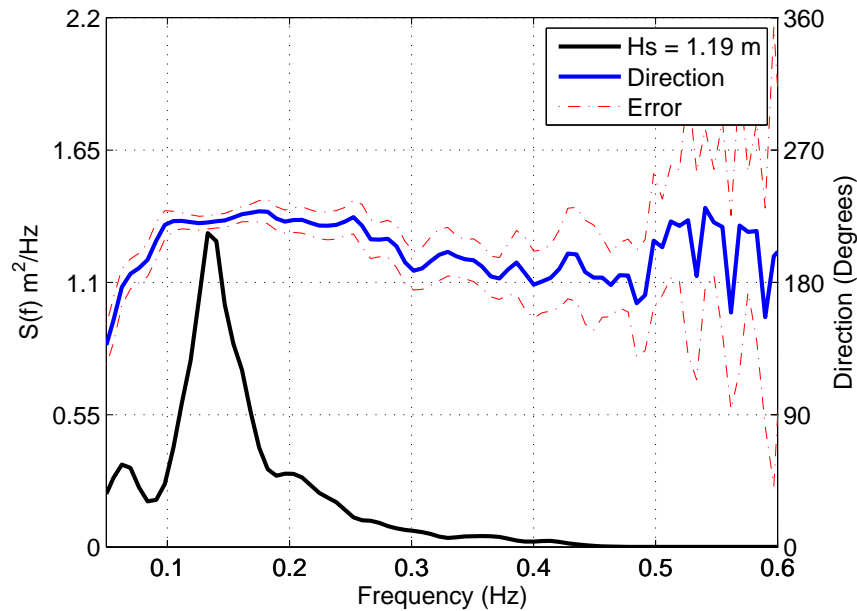


Figure 4-6: This figure shows the REMUS ADCP 3DM corrected wave height and mean wave direction. It is generated from data taken during the July 27th REMUS mission.

4.6 MVCO ADCP

As discussed in Chapter 2, the MVCO ADCP is a 1200 kHz RDI Sentinel broadband ADCP. The device continuously samples at 2 Hz. It is bottom-mounted at the MVCO 12 meter node.

MVCO ADCP data files are logged in 20 minute blocks and are saved to the MVCO ftp site. The files are saved in the standard format developed by RDI and a standard unpacker for PDO data was used to unpack the files into Matlab for post-processing.

MVCO ADCP data files contain the measured four beam velocities, intensities, correlations, and attitude and heading measurements from the on-board tilt sensors. Additional information regarding the ADCP configuration is also stored.

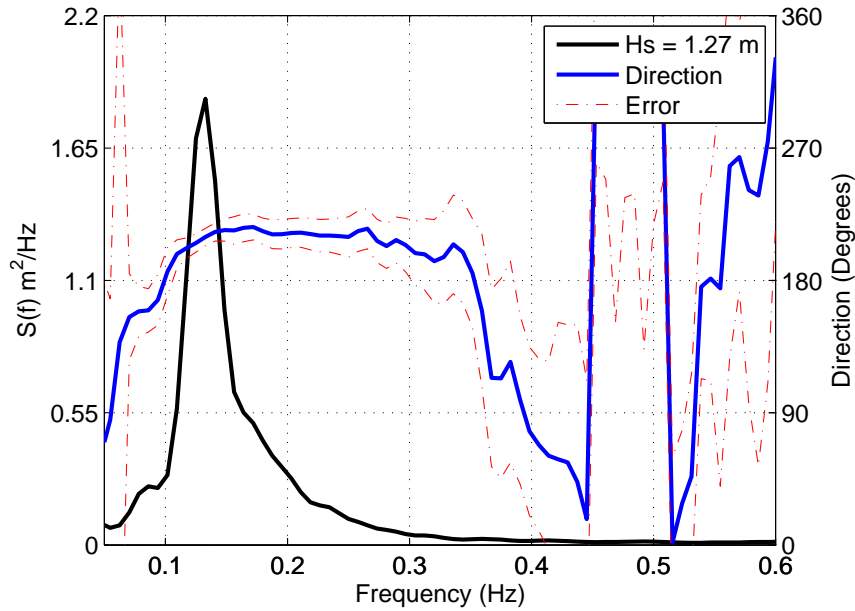


Figure 4-7: This figure represents the wave height and mean wave direction estimate produced by the MVCO ADCP. It is generated from data taken during the July 27th REMUS mission.

4.6.1 MVCO Processing Method

Data from the ADCP is initially analyzed for correlation and bad data. A low correlation threshold between beams is checked and any poorly correlated beams are flagged and removed by linear interpolation.

The MVCO ADCP data is analyzed using the “triplet” analysis outlined in Chapter 2. The wave velocities are rotated to the Earth’s coordinate frame using the on-board tilt sensors. The heading of the ADCP is known from installation and is hard coded into the processing routine. The height spectrum is directly derived from the individual beam velocity spectra, while the mean wave direction is derived from the cross spectra of the horizontal components of velocity with the vertical components.

Figure 4-7 shows an example height spectrum and mean wave direction estimate from the MVCO ADCP during the July 27th REMUS mission.

4.7 Datawell Waverider Buoy

The Datawell Waverider buoy was recovered on July 27th following the last REMUS mission. Wave spectral information and raw displacement data were continuously logged and stored on the internal SD card for the length of the deployment. Wave information was also transmitted via the ARGOS satellite system and via HF radio. The HF radio and ARGOS data was not used as it served only as a backup to the internally logged data.

4.7.1 Datawell Processing Method

The raw displacement data is stored in .RDT files which contain three days worth of buoy displacements broken into 30 minute segments. Additional wave information such as displacement standard error, correlations, skewness, and kurtosis of the wave displacements are included.

The spectral information is stored in .SDT files. These files contain both spectral information and system messages. They are recorded in monthly intervals and contain 30 minute blocks of spectral data. The height and directional spectrum are recorded, as well as significant wave height and GPS location.

The logged data is processed first in the W@ves21 software provided by Datawell. This allows for quick verification of the data as well as an initial check of the conditions during each REMUS mission.

Once the data is verified in the W@ves21 software, the data files are loaded into Matlab using an unpacker written by Paul Jesson from Naval Postgraduate School. The data is not altered in any way, it is simply loaded into Matlab to allow for plotting against spectra generated from other sensors.

Figure 4-8 shows an example of the height and directional spectrum estimated from the Waverider wave buoy during the July 27th mission.

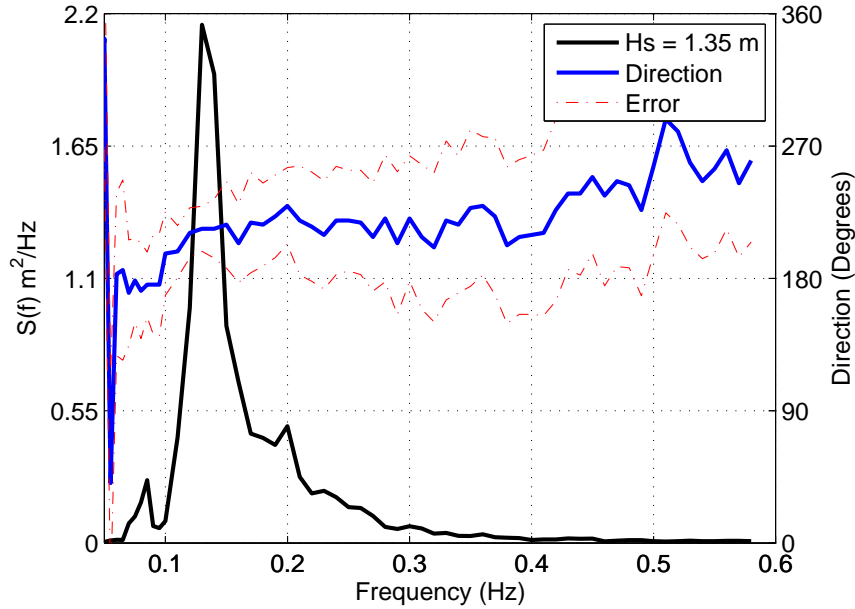


Figure 4-8: This plot shows an exported height and mean wave direction estimate generated by the Datawell Waverider Buoy. It is generated from data taken during the July 27th REMUS mission.

4.8 Doppler Correction

Because the vehicle is being propelled through the water (at an arbitrary direction relative to the waves), the apparent and intrinsic frequency of the waves differ by an amount known as the Doppler shift.

The relationship is

$$\omega_{intrinsic} = \omega_{apparent} + \mathbf{k} \cdot \mathbf{U} = \omega_{apparent} + |k||u| \cos \theta \quad (4.1)$$

where k is the wave number, u is the relative velocity between the vehicle and the waves. θ is the angle between the wave velocity vector and the vehicle velocity vector, and is determined by differencing the vehicle heading from the wave direction measured by the mean directional spread of the waves at the measured peak frequency of the height spectrum. The height spectrum is computed as a function of apparent frequency, and must be corrected to a function of intrinsic frequency.

Recall the dispersion relation discussed in Appendix B that links the relationship

between intrinsic frequency and wave number.

$$\omega^2 = gk \tanh(kh) \quad (4.2)$$

where h is the water depth. Substituting (4.1) into (4.2) gives

$$(\omega_{\text{apparent}} + |k||u| \cos \theta)^2 = gk \tanh(kh) \quad (4.3)$$

We solve this relation for the wave number, k , using a Matlab routine obtained from E. Terray (*personal communication*). Once the wave number has been determined, it can be substituted back into (4.2) to determine the instructor frequency.

The example spectra given in Figures 4-4 through 4-8 are Doppler corrected using the above method. Figure 4-9 shows an uncorrected and Doppler corrected height spectrum taken from data during a southern direction REMUS leg. This is the same data used in the bottom track correction example spectra shown in Figure 4-4.

During the mission, the waves were found to be coming from the south. While the vehicle was traveling on a southerly leg, the translational speed of the vehicle caused an up-shift in the apparent frequency of the measured spectrum. Using the known heading of the vehicle, and the estimated direction from the measured mean wave direction, the angle between the relative motion of the vehicle and waves is determined and the correct Doppler correction can be calculated and applied on each directional leg.

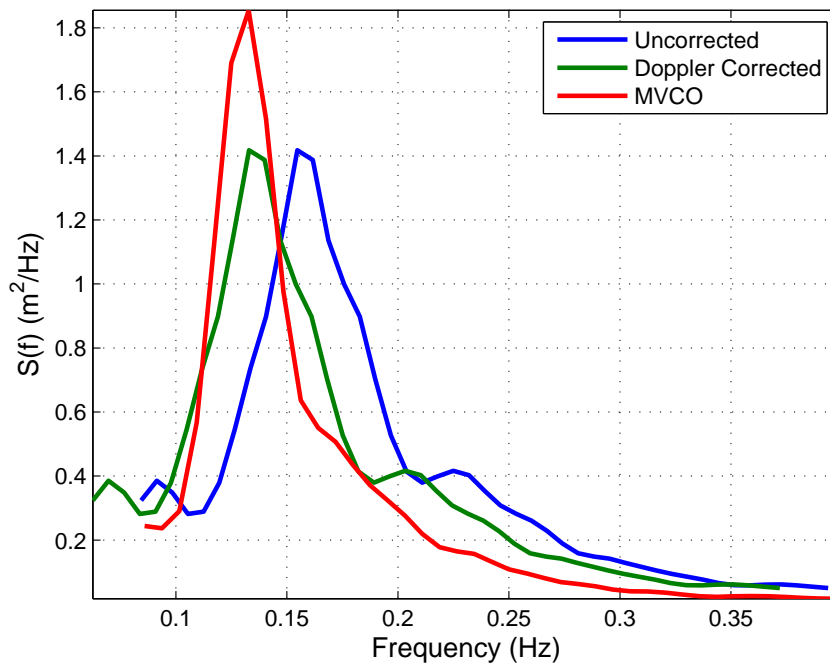


Figure 4-9: This figure shows the uncorrected and Doppler corrected height spectrum from the REMUS using bottom track velocity corrections. It is generated from data taken while the vehicle traveled along a southern leg during the July 27th REMUS mission. The apparent frequency is Doppler shifted up due to the relative velocity between the vehicle trajectory and wave direction.

Chapter 5

Sensor Comparison and Analysis

5.1 Introduction

The ultimate goal of this experiment was to develop the ability to measure wave height and direction from a moving underwater platform. In order to determine whether we were successful, the results have to be compared to a standard measurement technique that has already been validated.

We take the Datawell MK-III Directional Waverider buoy as the primary standard for this research. Additionally, the bottom mounted MVCO ADCP provides a useful comparison against a non-moving ADCP of the same frequency (1200 kHz) as is on the REMUS.

Wave spectra from the Waverider Buoy, MVCO ADCP, and REMUS ADCP are shown in the following sections to show the capability of each device to measure waves. Since the Waverider is used as the true benchmark, all statistics regarding deviation from the standard are in reference to deviations from the wave buoy.

5.2 Sensor to Sensor Data Comparisons

Numerous sensors providing redundant measurements were deployed during this experiment. For example, the Kearfott INU and Microstrain AHRS both measure the vector acceleration, attitude and heading of the vehicle. Comparing the outputs of

these sensors against one another further allows us to determine the most effective devices for measuring specific wave and vehicle information and allow for more flexibility during operations and planning.

5.2.1 3DM to Kearfott

The Microstrain 3DM sensor provides an exciting opportunity to test a low cost off-the-shelf AHRS in this application against the Kearfott INU. The latter is intended for navigation and has significantly smaller drift than the Microstrain device. Consequently, we consider that the Kearfott unit provides the comparison standard. Both systems directly measure attitude and heading, 3-axis accelerations, and 3-axis angular rates. The following sections provide quantitative results that show how well the 3DM compares with the Kearfott. Each section provides a snapshot of various outputs from each sensor while the vehicle is on a steady course. Additionally, each signal is band-pass filtered around the wave band to show how well each sensor can measure the wave induced motion of the vehicle.

In this chapter only single axis results from the July 27th mission are shown. Additional results for the other axis can be found in Appendix E.

Vehicle Accelerations

The ability to determine the vehicle velocity from an inertial sensor is critical in deep water when the ADCP bottom-track is not available. The Kearfott reports vehicle velocity directly, but the 3DM requires post-processing to estimate this quantity. The 3DM accelerations are leveled using the attitude reported by the instrument, high-pass filtered to remove low frequency noise, and integrated to obtain vehicle velocities. The 3DM also combines accelerations and angular rates using a complementary filter to estimate attitude.

Figure 5-1 shows a plot of the raw X-axis accelerometer data reported by the Microstrain and Kearfott sensors. The signals track exceptionally well together, with only a small offset in the mean value. This is most likely due to a small offset in

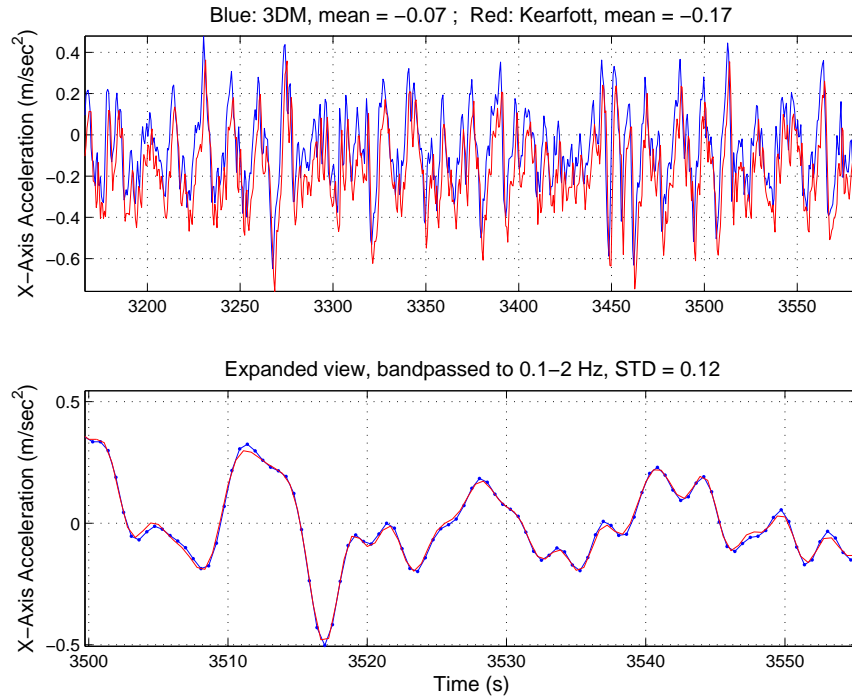


Figure 5-1: These plots show a snapshot of the raw 3DM (blue) and Kearfott (red) X-axis accelerometer signals. The lower plot is band-passed to show the wave induced accelerations in the wave band. STD is the standard deviation of the difference between the entirety of the two band-passed signals.

alignment between the Kearfott and 3DM instrument coordinate frames.

Angular Rates

As discussed above, the angular rates measured by the 3DM inertial sensor are an important part of the algorithm to compute vehicle attitude (via a complementary filter).

Figure 5-2 shows the angular rates from the 3DM and the Kearfott. The angular rates of the Kearfott and 3DM again track exceptionally well together in the wave band.

Vehicle Attitude and Heading

The complementary filter used in the 3DM to estimate vehicle attitude low-pass filters the accelerometers and integrates and high-pass filters the angular rates to determine

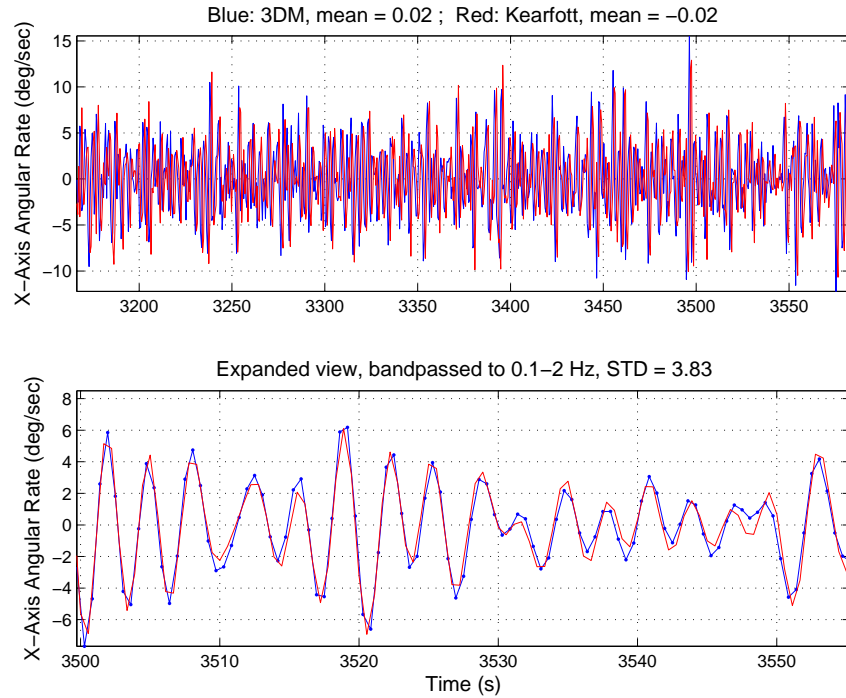


Figure 5-2: This figure shows the 3DM Angular rates in blue and the Kearfott angular rates in red. The bottom plot shows the band-passed angular rates.

pitch and roll. Additional information regarding the complementary filter used in the 3DM is discussed in Appendix F. Heading is determined from the projection of the vector magnetic field onto a level plane determined by the attitude calculation. The magnetometer measurement is easily biased by stray magnetic fields in the vicinity of the sensor (known as a “hard iron” effect), and by the presence of magnetically permeable material (known as a “soft iron” effect), which locally distorts the earth’s field. Both of these biases need to be calibrated prior to deployment, but after the sensor is installed. We were unable to perform this calibration prior to our last deployment, and so calibrated the 3DM’s magnetometer *in situ* against the Kerfott heading (which is based on a north-seeking gyro) by having the REMUS drive in a circle.

Figure 5-3 shows the measured heading from the 3DM and the Kearfott. Hard and soft iron calibrations were not performed prior to the vehicle deployment which resulted in the large offset in heading.

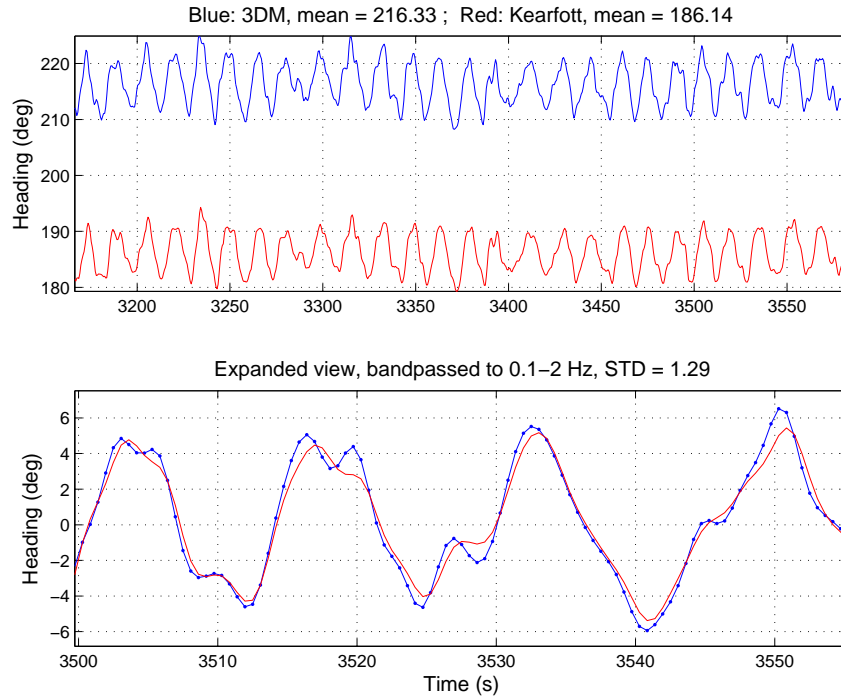


Figure 5-3: This figure shows the 3DM heading in blue and the Kearfott heading in red. The large offset in heading in the upper plot is due to hard and soft iron effects from the vehicle and surrounding equipment.

Velocities

The measured velocities of the 3DM and Kearfott are directly used to compensate for the motion of the vehicle. The 3DM velocities are determined by high-pass filtering and then integrating the accelerometer signals, as discussed above. The Kearfott velocities are directly reported from the INU.

Figure 5-4 shows the forward (X-axis) velocities from the 3DM and the Kearfott. The upper plot of 5-4 is different from previous comparisons as it shows filtered 3DM and Kearfott velocities, while the previous figures have shown unfiltered data in the upper plot. This is why there is no mean values listed at the top of the figure. The lower plot is a closer view of the same filtered signals. Unfiltered 3DM velocities are unable to be shown due to the fact that the velocities are generated by high-passing and integrating the 3DM accelerometer signals.

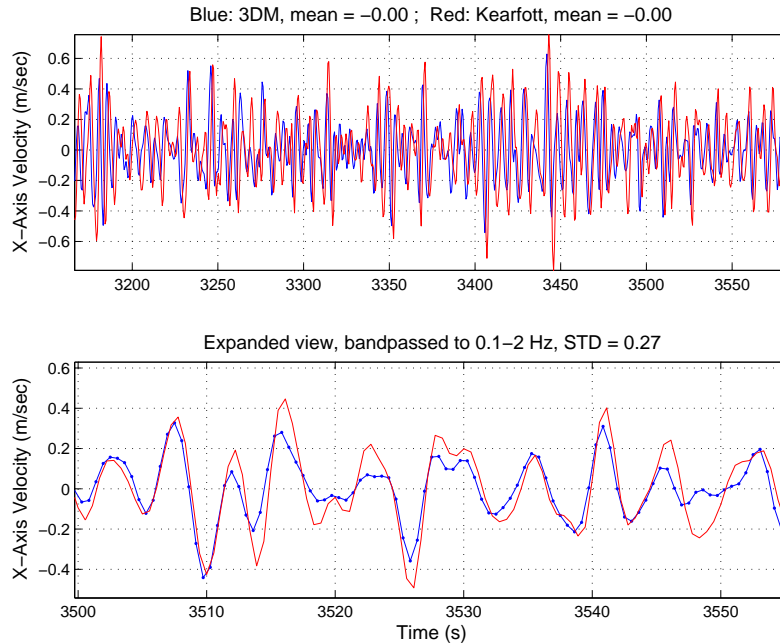


Figure 5-4: This figure shows the 3DM forward velocity in blue and the Kearfott forward velocity in red. The upper plot shows filtered velocities which has removed the mean values, while the lower plot shows a closer view of the filtered velocity signals.

5.2.2 ADCP to Kearfott

The ADCP directly measures the velocity of the vehicle relative to the sea bed using Doppler sonar. The Kearfott uses a Kalman filter to estimate velocity by combining accelerations and angular rates – the latter measured using ring laser gyros. While both methods are drastically different, both yield usable and accurate vehicle velocities that can be used to correct for the wave motion of the vehicle.

Velocities

Figure 5-5 shows the measured X-axis Kearfott and ADCP bottom track velocity. The agreement of the two signals is remarkable considering the different methods used to obtain the data.

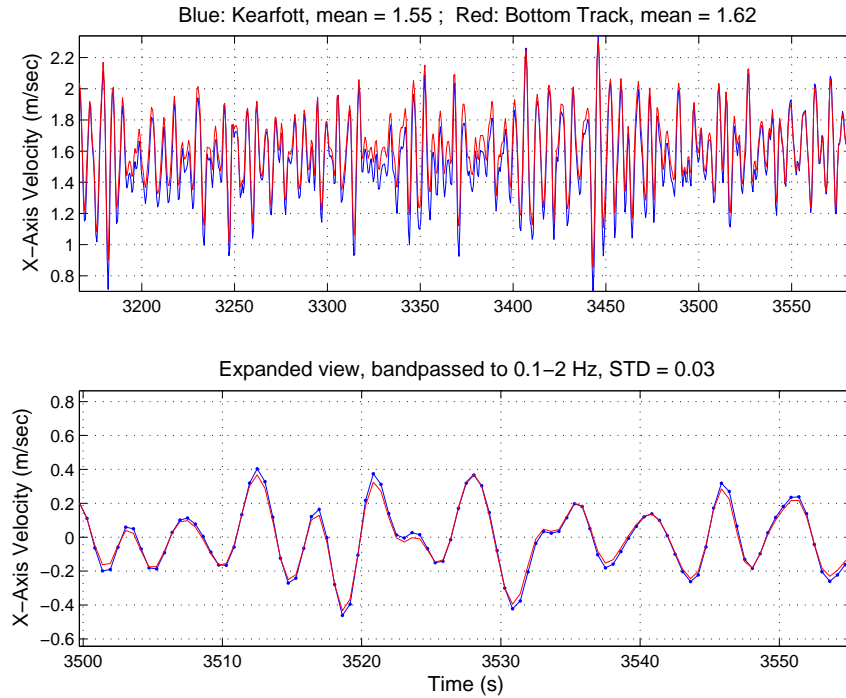


Figure 5-5: These plots show the measured X-axis (Forward) vehicle velocities as reported by the Kearfott (Blue) and ADCP bottom track (Red). The bottom plot shows band-passed filtered velocities to show the signal correlation in the wave band.

5.3 Spectral Comparison

Height spectra and mean wave direction estimates were developed from each deployed sensor. MVCO and Datawell spectra were estimated from individual time record files, while REMUS spectra were estimated over individual REMUS directional legs during the missions.

The following sections give height and mean wave direction estimates that show key points during each of the separate REMUS mission days. Appendix D provides more examples of height and directional estimates during each of the four directional legs of the REMUS missions.

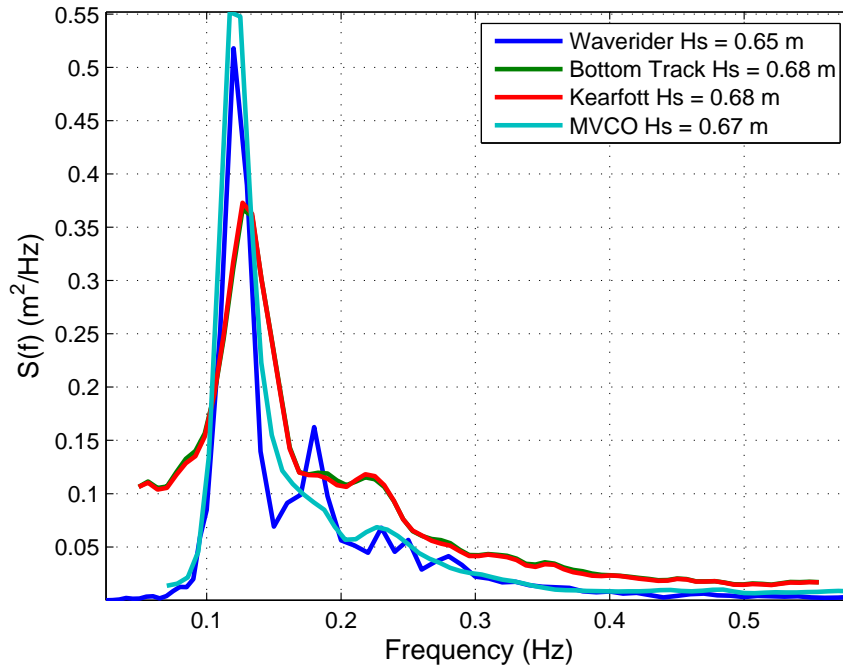


Figure 5-6: Height spectrum from all deployed sensors during the April 26th mission. This spectrum was specifically estimated from a southern leg.

5.3.1 Height Spectra

April 26th

Figure 5-6 shows the spectrum measured from the REMUS, Waverider, and MVCO during the April 26th mission. The REMUS spectra are generated from data recorded during a southern leg. The bottom track and Kearfott corrections yield almost identical spectra.

May 17th

Figure 5-7 shows spectral estimates from the May 17th mission. REMUS spectra were generated during a southern leg. This was the first mission with an operational 3DM, however the 3DM heading data was heavily biased and resulted in poor 3DM results.

The Kearfott and bottom track corrected spectra again proved to be very similar to the MVCO and Datawell spectra. Because the waves were coming from the south,

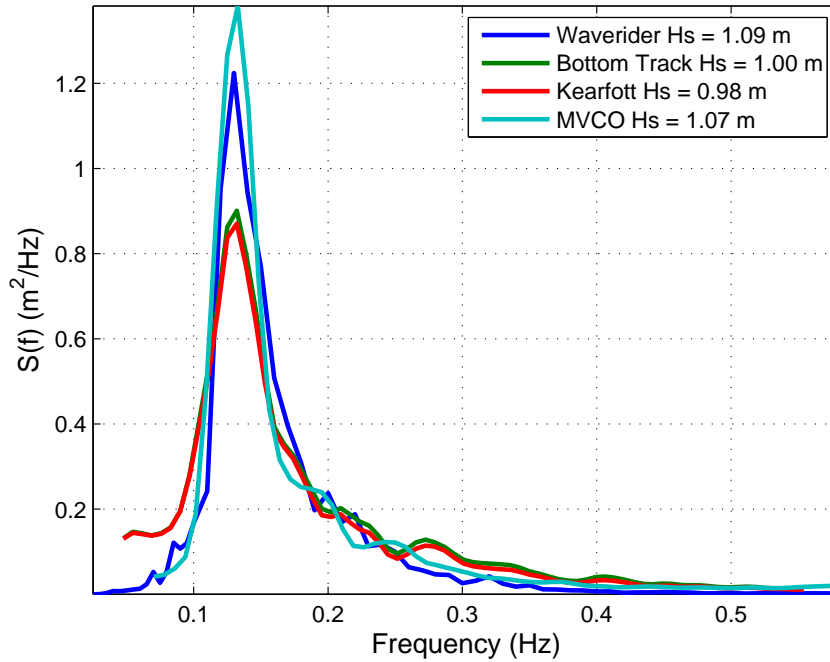


Figure 5-7: Height spectrum from all deployed sensors during the May 17th mission. This spectrum was specifically estimated from a southern leg.

the REMUS spectra had to be corrected to account for the Doppler-shift in frequency during an up-wave leg. The results shown in 5-7 use the Doppler correction method outlined in Chapter 4.

July 27th

Figure 5-8 shows spectra generated during the July 27th mission during a southern leg.

5.3.2 Mean Wave Direction

April 26th

Figure 5-9 shows the estimated mean wave direction generated by the sensors employed on the April 26th mission. The REMUS estimates are generated during an southern leg, and all estimates are within the Datawell directional spread.

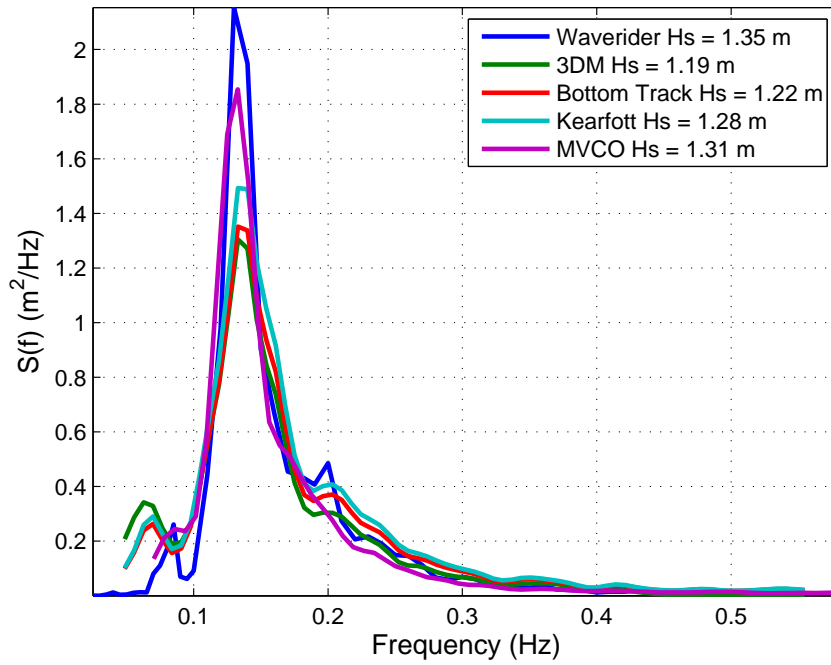


Figure 5-8: Height spectrum from all deployed sensors during the July 27th mission. This spectrum was estimated from a southern leg.

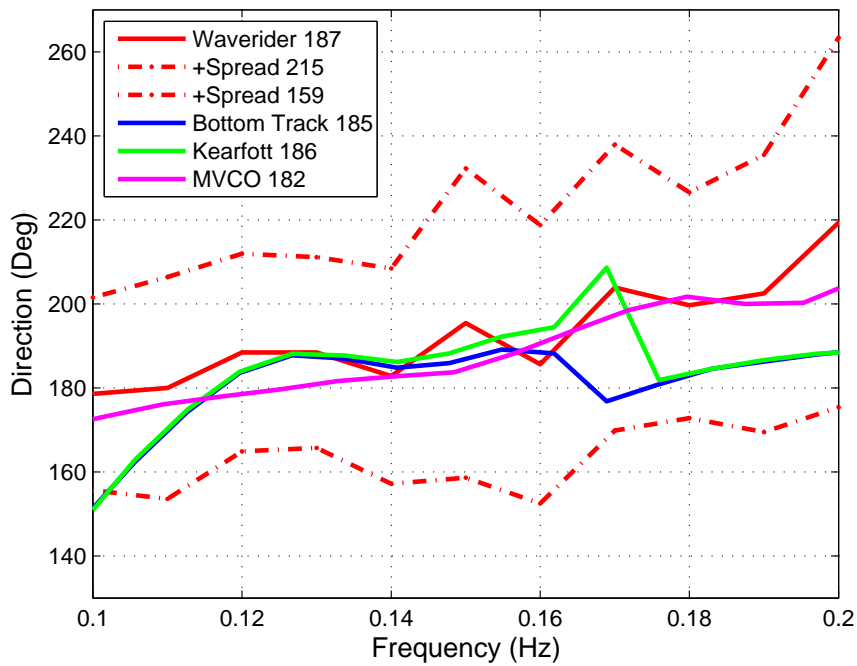


Figure 5-9: Mean wave direction estimate from all deployed sensors during the April 26th mission. This estimate was derived from data taken during a southern leg.

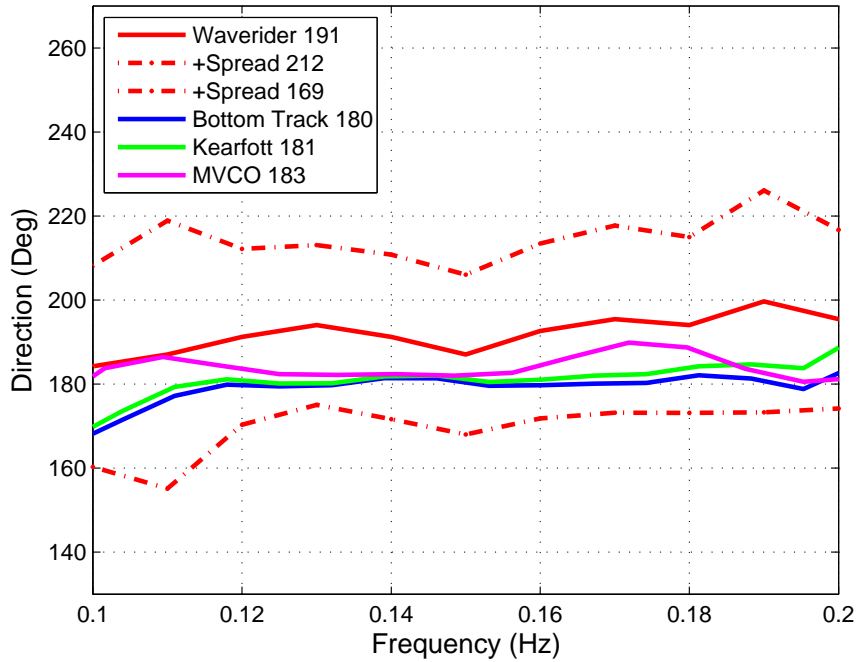


Figure 5-10: Mean wave direction from all deployed sensors during the May 17th mission. This estimate was derived from data taken during a southern leg.

May 17th

Figure 5-10 shows the estimated mean wave direction generated by the sensors employed on the May 17th mission. All sensors yield directional estimates that are within the spread of Waverider, although all the estimates show a slight offset of 5 to 10 degrees throughout the waveband.

July 27th

Figure 5-10 shows the estimated mean wave direction generated by the sensors employed on the July 27th mission. The REMUS spectra were generated during a southern leg.

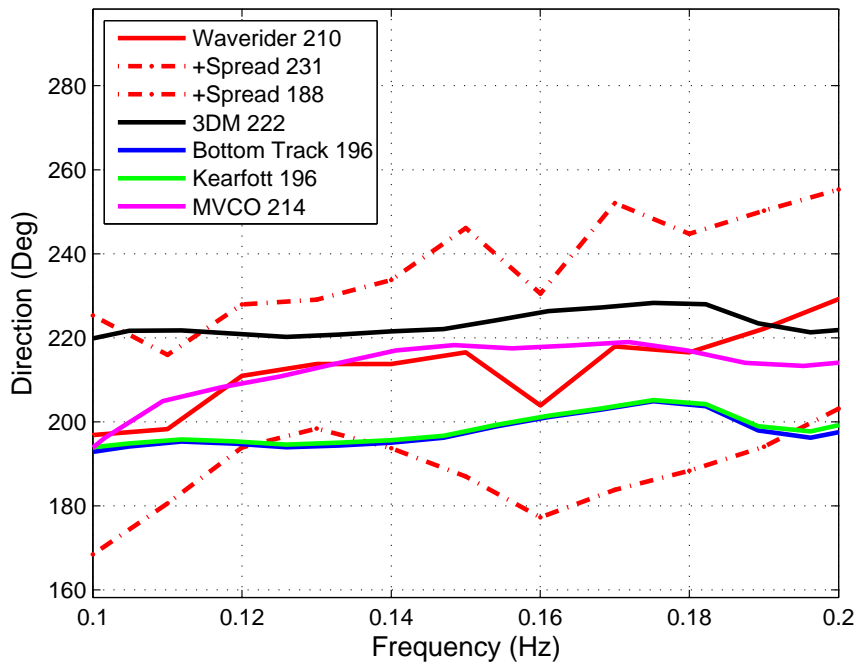


Figure 5-11: Mean wave direction from all deployed sensors during the July 27th mission. This estimate was derived from data taken during a southern leg.

Chapter 6

Summary and Conclusions

6.1 Summary

The work discussed here demonstrates that the non-directional spectrum of wave height and the mean wave direction as a function of frequency can be measured from an underway autonomous underwater vehicle in coastal depth waters. By using various inertial sensors and the bottom track capability of the ADCP, we show that the wave-induced vehicle motion can be successfully removed from the ADCP wave velocity record and that accurate estimates of the surface wave height and direction can be obtained. Additionally, the measured mean wave direction can be used directly to compensate for the Doppler shifted frequency of the waves induced by the translational velocity of the vehicle.

This is the first time that both wave direction and height spectra have been successfully measured from a moving underwater platform using an ADCP. This will allow for vehicles already equipped with an ADCP, such as REMUS, to provide a wealth of new information and data regarding surface ocean waves and their characteristics. By showing that the Microstrain AHRS, a low cost alternative to the Kearfott INU, is still able to provide accurate wave information, only small upgrades to current systems are necessary to be able to take advantage of this new AUV capability.

This research has shown that in shallow water where bottom track is available,

the best performing equipment lineup involves using the ADCP bottom track for velocity corrections and the Kearfott INU for heading and attitude corrections. Replacing the Kearfott with the 3DM shows only a minor reduction in wave direction accuracy, making the 3DM and ADCPs the most cost effective setup for an AUV in shallow water. Moving into deep water where bottom track is unavailable, the Kearfott supplies significantly improved velocity corrections over the 3DM, yet this translates into only marginal improvements in wave direction measurements. This allows an AUV equipped with only an upward looking ADCP and 3DM to provide accurate wave direction measurements. This configuration would also prove to be the most cost effective when applied to a subsurface mooring. In order to apply this capability to naval submarines, only an upward looking ADCP installed in the sail would be required, as the system would be able to interface directly with the ship's inertial navigation system for velocity, heading, and attitude adjustments. Table 6.1 gives a brief outline of the recommended platform, environment, and recommended equipment necessary for accurate estimates of wave height and direction.

Table 6.1: Platform and Recommended Sensors for Accurate Wave Analysis

Platform	Environment	ADCP	Sensors
AUV	Deep	Upward ADCP	Kearfott
	Shallow	DVL	Bottom Track and 3DM
Subsurface Float	Both	Upward ADCP	3DM
Naval Submarine	Both	Upward ADCP	Shipboard INS

6.2 Future Work

This technology has numerous applications and potential for future research and investigation. Due to the limited time and scope of the work presented in this thesis, all avenues of research regarding different operating environments and their impact on the wave measuring capabilities were not fully explored. Additionally, different processing techniques were discussed but never formally implemented due to the relatively short time frame of this project.

6.2.1 Environmental Work

This experiment was ultimately limited by the geography of the location where the wave buoy was deployed because the primary wave direction was always from the south and the period of the energy-containing waves was in the range of 6 to 8 seconds.

Future work in different environments could further justify our results. Operations in deeper water would allow for the vehicle to run deeper and investigate further the error associated with beam separation. Operations in water where the mean wave direction comes from more than one direction would also serve to verify our findings.

Any future testing done in environmental conditions outside of those commonly found south of Martha's Vineyard would help to confirm our results and validate the technology as an acceptable method for wave measurement.

6.2.2 Wavelet Analysis

Another method of processing that would allow for more accurate representation of the wave spectra, particularly for multi-directional seas, could be through the use of wavelet analysis.

Work by Donelan et al. (1996); Krogstad et al. (2006) shows exciting new ways to think about and process wave data using wavelet methods. Barreira and Ribeiro (2011) specifically adapt wavelet processing methods to ADCPs. Applying this processing method to a moving vehicle ADCP could further reduce the errors associated with the moving platform.

An attempt was made early on to apply wavelet processing techniques in this project, but the processing routines proved to be far too challenging for the time available.

6.2.3 Subsurface Moorings

As discussed before, work done by Wood et al. (2005) used an upward and downward looking ADCP to measure waves from a subsurface mooring. While they were successful, reducing the cost by only requiring an upward looking ADCP and inertial

measurement system for velocity, attitude, and heading corrections would allow for easier wave measurement systems without the need of a second ADCP.

6.2.4 Naval Submarine Employment

As a Naval Submariner, my initial interest in the project was to be able to provide real time wave information to the crew of naval submarines while submerged. I have first hand experience regarding the challenging scenarios that naval submarine ship control parties face while maintaining depth control in an unknown sea state. While understanding wave conditions is not the only component of a successful mission at periscope depth, it can be a valuable piece of information that allows the Officer of the Deck to make the most informed decision regarding the best course for operations.

I foresee this technology being easily installed and maintained by a submarine crew. The ADCP could be installed in the sail, flush with the surface. The system would interface directly with the shipboard navigation system, allowing for the most accurate speed, attitude, and heading corrections available. A small indication panel could be installed in the control room, within plain view of the ship's control party and the Officer of the Deck. A watch stander would be responsible for energizing and securing of the system prior to periscope depth operations, and would make appropriate reports regarding the status of the system to the Officer of the Deck. All of this would require only limited training regarding the systems operation and would provide another valuable sensor to the ship's Captain and crew.

There are numerous steps that would need to occur before this system could be employed. Specific testing regarding counter detection would be essential. Active sonar, in any form or frequency, requires thorough investigation to determine the counter-detection range of its signal. While the ADCP used in this research transmits a 1200 kHz signal which has very limited range, actual testing of its transmit range would be required prior to use on a Naval vessel. Additionally, work regarding the interfacing of the ADCP with the ship's inertial navigation system would require extensive testing and permission.

6.3 Conclusion

We have shown that it is possible to measure ocean wave height and direction using an ADCP from a moving underway AUV. Given the right sensors, corrections can be made to the ADCP wave velocity record that allow for accurate estimations of mean wave direction and height. REMUS vehicles are already equipped with most of the tools required for accurate wave measurement. In the event a REMUS vehicle does not have a Kearfott or other inertial navigation system, we show that the much lower cost Microstrain 3DM-GX3-25 AHRS is adequate to provide platform velocity, attitude, and heading. Although we demonstrated the method using a small AUV, we believe that it is immediately transferable to larger underwater vehicles, such as submarines, as well as to underwater moorings. The latter application would permit ADCP measurements of waves in arbitrary water depths.

Appendix A

The Doppler Effect

A.1 Introduction

In 1842, Christian Doppler published a paper describing how the color of a binary star moving across the sky changed based on the relative motion between the star and the observer. This phenomenon, termed the Doppler effect, describes how the observed frequency of a wave changes based on the relative speed between the source and observer. The most common description of this effect is that of a siren on a fire truck. As the fire truck drives towards the observer, the received pitch, or frequency appears to increase. The frequency reaches its maximum when the fire truck reaches its closest point to the observer, and then the frequency falls off as the fire trucks increases the range between the observer and the siren.

A.2 Derivation

Figure A-1 (a) shows the wavelength, λ , of a signal with a transmitted frequency, f_t , and received frequency, f_r . The wave propagates at speed, c , where

$$c = f_t \lambda \tag{A.1}$$

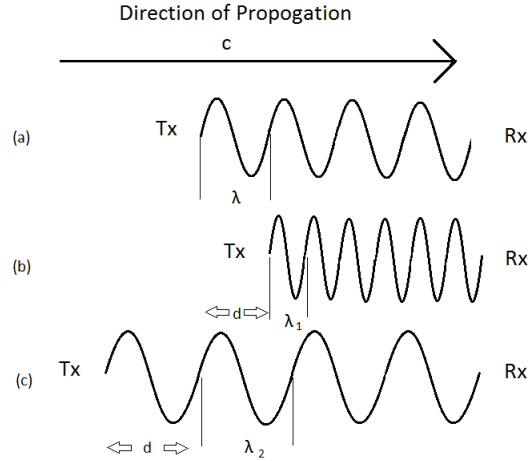


Figure A-1: Doppler effect seen by moving the source closer and further from the receiver. T_x is the transmitter, R_x is the receiver, λ is the wavelength, and d is the distance moved from the original position.

Figure A-1 (b) shows the transmitter being moved towards the receiver by a distance of d where

$$d = v/f_t \quad (\text{A.2})$$

and v is the velocity of the transmitter. Therefore the observed wavelength is

$$\lambda_1 = \lambda - v/f_t \quad (\text{A.3})$$

and the observed frequency is

$$f_{r1} = f_t \left(\frac{c}{c - v} \right) \quad (\text{A.4})$$

Similarly, Figure A-1 (c) shows the transmitter being moved away from the receiver by a distance of d . The observed wavelength for this case is

$$\lambda_2 = \lambda + v/f_t \quad (\text{A.5})$$

and the observed frequency is

$$f_{r2} = f_t \left(\frac{c}{c + v} \right) \quad (\text{A.6})$$

If the receiver was instead being moved toward the transmitter, the observed frequency would be

$$f_r = f_t \left(\frac{c + v}{c} \right) \quad (\text{A.7})$$

or if the receiver was moving away from the transmitter, the observed frequency would be

$$f_r = f_t \left(\frac{c - v}{c} \right) \quad (\text{A.8})$$

The measured Doppler shift f_d between the two signals is given by

$$f_d = f_r - f_t \quad (\text{A.9})$$

substituting (A.4) into (A.9) yields

$$f_d = f_t \left(\frac{v}{c} \right) \quad (\text{A.10})$$

A.3 ADCP Application

The ADCP relies on the acoustic signal backscattering off of small particles floating in the water column that are assumed to move at the same velocity as the water itself. This effect causes the ADCP to initially act as the transmitter and the back scattering particle to act as the receiver. In turn, the particle then becomes the source and the ADCP becomes the receiver. This causes the Doppler effect to be doubled.

$$f_d = 2f_t \left(\frac{v}{c} \right) \quad (\text{A.11})$$

Additionally, since the Doppler effect only applies to the radial motion between the transmitter and receiver, an additional angular term is added

$$f_d = 2f_t \left(\frac{v}{c} \right) \cos(\theta) \quad (\text{A.12})$$

where θ is the angle between the relative velocity vector and the line between the source and receiver. By maintaining a constant transmit frequency, and measuring the Doppler shifted return frequency, the ADCP is able to determine the radial velocity between the ADCP and the scattering particle along each beam.

Appendix B

Water Wave Mechanics

B.1 Introduction

This appendix focuses on surface gravity wave mechanics and is provided to establish some basic concepts regarding ocean wave analysis. The following sections give a brief introduction to linear and random wave theory and the ideas behind spectral estimation and analysis. Additional reading and information can be found in Kundu (1990); Dean and Dalrymple (1991)

B.2 Linear Wave Theory

The foundations of linear wave theory revolve around the implementation and solving of a boundary value problem. In these problems, a differential equation is defined that describes a specific system, in this case, the ocean. Boundary conditions are then established to find solutions to the differential equation that relate directly to the system at hand.

Some assumptions are made about the ocean fluid and its properties during the following sections. Those assumptions are that the water can be treated as an incompressible fluid, and that all flow is considered irrotational. The basis for these assumptions can be found in Kundu (1990).

The general form for the displacement of a plane wave on the surface of a fluid is of the form

$$\eta(\mathbf{x}, t) = a \sin(\mathbf{k}\mathbf{x} - \omega t) \quad (\text{B.1})$$

where a is the wave amplitude, \mathbf{k} is the wavenumber and ω is the radial frequency of the wave.

B.2.1 The Laplace Equation

Assuming that water is an incompressible fluid, the conservation of mass equation, or simply the continuity equation, can be written as

$$\frac{\partial u}{\partial x} + \frac{\partial v}{\partial y} + \frac{\partial w}{\partial z} = 0 \quad (\text{B.2})$$

Assuming the motion of the waves is irrotational, a velocity potential that satisfies the continuity equation can be written as

$$\begin{aligned} u &= \frac{\partial \varphi}{\partial x} \\ v &= \frac{\partial \varphi}{\partial y} \\ w &= \frac{\partial \varphi}{\partial z} \end{aligned} \quad (\text{B.3})$$

Substituting (B.3) into (B.2) gives the Laplace Equation.

$$\frac{\partial^2 \varphi}{\partial x^2} + \frac{\partial^2 \varphi}{\partial y^2} + \frac{\partial^2 \varphi}{\partial z^2} = 0 \quad (\text{B.4})$$

Assuming the waves only propagate in the x direction only, and that the motion takes place only in the $x - z$ plane, (B.4) simplifies to

$$\frac{\partial^2 \varphi}{\partial x^2} + \frac{\partial^2 \varphi}{\partial z^2} = 0 \quad (\text{B.5})$$

B.2.2 Boundary Conditions

Boundary conditions are required to be defined at the system boundaries in order to solve the governing differential equation. These boundary conditions impose physical and kinematic restraints on the system to allow for solutions that actually pertain to the system at hand. In the case of waves, three boundary conditions are established that allow us to solve the Laplace Equation and develop a solution that characterizes surface gravity waves.

Bottom Boundary Condition

The bottom boundary condition requires that the bottom of the system, in this case the ocean floor, does not move, therefore not allowing for any vertical velocity. This is written as

$$w = \frac{\partial \varphi}{\partial z} = 0 \quad \text{at} \quad z = -H \quad (\text{B.6})$$

Kinematic Free Surface Boundary Condition

The kinematic free surface boundary condition, or the kinematic boundary condition, requires that the fluid particles at the surface never leave the surface. This can be expressed as

$$\frac{\partial \eta}{\partial t} + u \frac{\partial \eta}{\partial x} = w \quad \text{at} \quad z = \eta \quad (\text{B.7})$$

By using dimensional analysis and scaling, Krogstad and Arntsen (2000) linearize the surface boundary conditions and shows that the second term of (B.7) is an order of magnitude smaller than the first and third terms and can therefore be neglected. (B.7) then simplifies to the linearized form of

$$\frac{\partial \eta}{\partial t} = w \quad \text{at} \quad z = 0 \quad (\text{B.8})$$

Dynamic Boundary Condition

The dynamic boundary condition requires that the pressure just below the free surface of the air-water interface be equal to the ambient pressure. This can be expressed as

$$\frac{\partial\varphi}{\partial t} + \frac{1}{2}(u^2 + w^2) + g\eta = 0 \quad \text{at} \quad z = \eta \quad (\text{B.9})$$

Similar to the method used to linearize the kinematic boundary condition, Krogstad and Arntsen (2000) again show that the second term of (B.9) is an order of magnitude smaller and can be ignored, thus resulting in the linearized dynamic boundary condition in the form of

$$\frac{\partial\varphi}{\partial t} + g\eta = 0 \quad \text{at} \quad z = 0 \quad (\text{B.10})$$

B.2.3 Solution of the Boundary Value Problem

To solve for the velocity potential, a generalized solution of the Laplace equation is used to develop the final solution. The generalized solution is of the form

$$\varphi = A(z) \sin(kx - \omega t) \quad (\text{B.11})$$

Substituting (B.11) into the 2 dimensional Laplace equation (B.5) gives

$$A(z)k^2 + \frac{\partial^2 A(z)}{\partial z^2} = 0 \quad (\text{B.12})$$

This second order ordinary differential equation has the general solution of

$$A(z) = C_1 e^{kz} + C_2 e^{-kz} \quad (\text{B.13})$$

Substituting (B.13) into (B.11) gives

$$\varphi = (C_1 e^{kz} + C_2 e^{-kz}) \sin(kx - \omega t) \quad (\text{B.14})$$

Boundary conditions are applied to solve for C_1 and C_2 . Applying the bottom boundary condition (B.6) to (B.14) yields

$$C_1 = C_2 e^{2kH} \quad (\text{B.15})$$

and applying the kinematic boundary condition (B.7) to (B.14) gives

$$k(C_1 - C_2) = a\omega \quad (\text{B.16})$$

Solving for C_1 and C_2 from (B.15) and (B.16) gives

$$C_1 = \frac{a\omega}{k} \frac{e^{2kH}}{(e^{2kH} - 1)} \quad (\text{B.17})$$

$$C_2 = \frac{a\omega}{k} \frac{1}{(e^{2kH} - 1)} \quad (\text{B.18})$$

Substituting C_1 (B.17) and C_2 (B.18) back into (B.14) gives

$$\varphi = \frac{a\omega}{k} F(kz) \sin(kx - \omega t) \quad (\text{B.19})$$

where $F(kz)$ is the vertical structure function given by

$$F(kz) = \frac{e^{k(2H+z)} + e^{-kz}}{e^{2kH} - 1} = \frac{\cosh(k(z + H))}{\sinh(kH)} \quad (\text{B.20})$$

From (B.19) the component wave velocities can be derived and are given by

$$u = a\omega F(kz) \cos(kx - \omega t) \quad (\text{B.21})$$

$$w = a\omega F'(kz) \sin(kx - \omega t) \quad (\text{B.22})$$

and finally, substituting (B.19) and (B.1) into the dynamic boundary condition (B.9) give

$$\omega^2 = gk \tanh(kH) \quad (\text{B.23})$$

which is the dispersion relation that describes how angular frequency and wave number are linked.

B.3 Random Wave Theory

Instead of considering a single plane wave traveling on the surface of the ocean, we now consider a finite number of plane waves traveling in a finite number of directions. This random surface is more reminiscent of the ocean surface that we are used to visualizing and can be expressed as

$$\eta(\mathbf{x}, t) = \sum_{n=1}^N a_n \sin(\mathbf{k}_n \mathbf{x} - \omega t + \phi_n) \quad (\text{B.24})$$

B.3.1 Wavenumber Spectrum

The expectation of the random surface can be expressed as

$$\mathbb{E}(a_n \sin(\mathbf{k}_n \mathbf{x} - \omega t + \phi_n)) = \frac{1}{2\pi} \int_0^{2\pi} a_n \sin(\mathbf{k}_n \mathbf{x} - \omega t + \phi_n) d\phi = 0 \quad (\text{B.25})$$

$$\mathbb{E}(\eta(\mathbf{x}, t)) = \sum_{n=1}^N \mathbb{E}(a_n \sin(\mathbf{k}_n \mathbf{x} - \omega t + \phi_n)) = 0 \quad (\text{B.26})$$

and the variance of the random surface is

$$\text{Var}(a_n \sin(\mathbf{k}_n \mathbf{x} - \omega t + \phi_n)) = \mathbb{E}(a_n \sin(\mathbf{k}_n \mathbf{x} - \omega t + \phi_n))^2 = \frac{a_n^2}{2} \quad (\text{B.27})$$

$$\text{Var}(\eta(\mathbf{x}, t)) = \mathbb{E}(\eta^2(\mathbf{x}, t)) = \sum_{n=1}^N \frac{a_n^2}{2} \quad (\text{B.28})$$

Assuming that the phase of the random surface is a uniformly distributed stochastic variable on the range of $[0, 2\pi]$, and that instead of a finite number, an infinite number of plane waves is considered, the wave number spectrum can be defined by

$$\text{Var}(\eta(\mathbf{x}, t)) = \int_k \Psi(\mathbf{k}) d^2 \mathbf{k} \quad (\text{B.29})$$

B.3.2 Directional Wave Spectrum

Expressing the wavenumber spectrum in polar coordinates and substituting the wavenumber k for the angular frequency ω the wavenumber spectrum can then be expressed as

$$Var(\eta(\mathbf{x}, t)) = \int_{\mathbf{k}} \Psi(\mathbf{k}) d^2\mathbf{k} = \int_{k=0}^{\infty} \int_{\theta=0}^{2\pi} \Psi(k, \theta) k dk d\theta \quad (\text{B.30})$$

$$Var(\eta(\mathbf{x}, t)) = \int_{\omega=0}^{\infty} \int_{\theta=0}^{2\pi} \Psi(k(\omega), \theta) k(\omega) \frac{dk}{d\omega} d\omega d\theta \quad (\text{B.31})$$

$$Var(\eta(\mathbf{x}, t)) = \int_{\omega=0}^{\infty} \int_{\theta=0}^{2\pi} E(k, \theta) d\omega d\theta \quad (\text{B.32})$$

The function

$$E(k, \theta) = \Psi(k(\omega), \theta) k(\omega) \frac{dk}{d\omega} \quad (\text{B.33})$$

is called the directional wave spectrum and contains information regarding the direction of the waves. The directional wave spectrum can then be further reduced to

$$E(k, \theta) = S(\omega) D(\omega, \theta) \quad (\text{B.34})$$

where $S(\omega)$ is the wave frequency spectrum and $D(\omega, \theta)$ is the directional distribution.

The directional distribution is often normalized by

$$\int_{\theta=0}^{2\pi} D(\omega, \theta) d\theta = 1 \quad \text{for all } \omega \geq 0 \quad (\text{B.35})$$

It is from this directional distribution that the wave mean direction is able to be determined. This process is discussed in Chapter 2.

Appendix C

Spectral Analysis

C.1 Introduction

Appendix B introduces some linear wave theory, the wave frequency spectrum, $S(\omega)$, and the directional spectrum, $D(\theta, \omega)$. This appendix employs the linear wave theory discussed in Appendix B and derives the methods used to convert the measured beam velocities from the ADCP into estimates of the wave height and mean wave direction.

C.2 Height Spectra Analysis

Starting with the linear wave theory discussed in Appendix B, the surface displacement and velocity potential functions for a wave field are given by

$$\eta = ae^{i(\mathbf{k}\cdot\mathbf{x}-\omega t)} \quad (\text{C.1})$$

$$\varphi = -\frac{i\omega}{k}F(kz)\eta \quad (\text{C.2})$$

The positional derivatives of the velocity potential yield the three dimensional wave component velocities and are given by

$$U = \omega \cos(\theta)F(kz)\eta \quad (\text{C.3})$$

$$V = \omega \sin(\theta)F(kz)\eta \quad (\text{C.4})$$

$$W = -i\omega F'(kz)\eta \quad (\text{C.5})$$

Each ADCP beam measures a component of the vertical and horizontal wave orbital velocity. The measured ADCP beam velocities are given by

$$u_1 = U \sin \alpha + W \cos \alpha \quad (\text{C.6})$$

$$u_2 = -U \sin \alpha + W \cos \alpha \quad (\text{C.7})$$

$$v_1 = V \sin \alpha + W \cos \alpha \quad (\text{C.8})$$

$$v_2 = -V \sin \alpha + W \cos \alpha \quad (\text{C.9})$$

where α is the beam angle between the vertical axis and the transducer face.

Substituting the wave velocity components into the beam velocities yields

$$u_1 = \omega \cos(\theta)F(kz)\eta \sin \alpha - i\omega F'(kz)\eta \cos \alpha \quad (\text{C.10})$$

$$u_2 = -\omega \cos(\theta)F(kz)\eta \sin \alpha - i\omega F'(kz)\eta \cos \alpha \quad (\text{C.11})$$

$$v_1 = \omega \sin(\theta)F(kz)\eta \sin \alpha - i\omega F'(kz)\eta \cos \alpha \quad (\text{C.12})$$

$$v_2 = -\omega \sin(\theta)F(kz)\eta \sin \alpha - i\omega F'(kz)\eta \cos \alpha \quad (\text{C.13})$$

Recall that the covariance between two signals is given by

$$C_{ij}(\tau) = \frac{1}{T} \int_t^{t+\tau} f_i(t)f_j(t+\tau)dt \quad (\text{C.14})$$

$$C_{ij}(\tau) = \hat{f}_i^*(n)\hat{f}_j(n)e^{in\omega\tau} \quad (\text{C.15})$$

The power spectrum is then defined as the Fourier transform of the covariance function.

$$S_{ij}(n) = \frac{1}{T} \int_t^{t+\tau} C_{ij}e^{-in\omega t}d\tau \quad (\text{C.16})$$

$$S_{ij}(n) = \hat{f}_i^*(n)\hat{f}_j(n) \quad (\text{C.17})$$

The power spectra of the beam velocities are then given by

$$S_{u_1} = [\omega^2 \cos^2(\theta) F(kz)^2 \sin^2 \alpha^2 + \omega^2 F'(kz)^2 \cos^2 \alpha^2] S_\eta \quad (\text{C.18})$$

$$S_{u_2} = [\omega^2 \cos^2(\theta) F(kz)^2 \sin^2 \alpha^2 + \omega^2 F'(kz)^2 \cos^2 \alpha^2] S_\eta \quad (\text{C.19})$$

$$S_{v_1} = [\omega^2 \sin^2(\theta) F(kz)^2 \sin^2 \alpha^2 + \omega^2 F'(kz)^2 \cos^2 \alpha^2] S_\eta \quad (\text{C.20})$$

$$S_{v_2} = [\omega^2 \sin^2(\theta) F(kz)^2 \sin^2 \alpha^2 + \omega^2 F'(kz)^2 \cos^2 \alpha^2] S_\eta \quad (\text{C.21})$$

The non directional wave frequency spectrum S_η can then be solved for by the individual beam velocities and is given by

$$S_\eta = \frac{S_{u_1} + S_{u_2} + S_{v_1} + S_{v_2}}{2\omega^2(F(kz)^2 \sin^2 \alpha^2 + 2F'(kz)^2 \cos^2 \alpha^2)} \quad (\text{C.22})$$

C.3 Mean Wave Direction Analysis

The directional coefficients, c_n are defined as the Fourier coefficients in the expansion of the frequency-direction spectrum, $D(\omega, \theta)$, in circular harmonics

$$D(\omega, \theta) = \frac{1}{2\pi} \sum_{n=-\infty}^{+\infty} c_n(\omega) \exp(-in\theta) \quad (\text{C.23})$$

Inverting this relation gives

$$c_n(\omega) = \int_{-\pi}^{+\pi} d\theta D(\omega, \theta) \exp(in\theta) \quad (\text{C.24})$$

The directional coefficients are complex, and it is conventional to write c_n in terms of its real and imaginary parts as

$$c_n = a_n + ib_n \quad (\text{C.25})$$

so that

$$a_n = \overline{\cos(n\theta)} \quad \text{and} \quad b_n = \overline{\sin(n\theta)} \quad (\text{C.26})$$

Taking the auto and cross power spectra of the wave velocity components gives

$$S_w = \omega^2 F'(kz)^2 S_\eta \quad (\text{C.27})$$

$$S_u = \omega^2 \cos^2(\theta) F(kz)^2 S_\eta \quad (\text{C.28})$$

$$S_v = \omega^2 \sin^2(\theta) F(kz)^2 S_\eta \quad (\text{C.29})$$

$$S_{wu} = -i\omega^2 \cos(\theta) F(kz) F'(kz) S_\eta \quad (\text{C.30})$$

$$S_{wv} = -i\omega^2 \sin(\theta) F(kz) F'(kz) S_\eta \quad (\text{C.31})$$

$$S_{uv} = \frac{1}{2} \omega^2 F(kz)^2 \sin(2\theta) S_\eta \quad (\text{C.32})$$

The first four Fourier coefficients are then given by

$$a_1 = \frac{Q_{wu}}{\sqrt{S_w(S_u + S_v)}} \quad (\text{C.33})$$

$$b_1 = \frac{Q_{wv}}{\sqrt{S_w(S_u + S_v)}} \quad (\text{C.34})$$

$$a_2 = \frac{S_u - S_v}{S_u + S_v} \quad (\text{C.35})$$

$$b_2 = \frac{2S_{uv}}{S_u + S_v} \quad (\text{C.36})$$

where $S_{wu} = -iQ_{wu}$ and $S_{wv} = -iQ_{wv}$

The quantities a_1 and b_1 give an estimate of the mean wave direction at each frequency as

$$\bar{\theta} = \text{atan2}(b_1, a_1) \quad (\text{C.37})$$

Appendix D

Mission Results and Data

D.1 Mission Results and Comparison

This appendix provides the wave height spectra and mean wave direction estimates found during each of the REMUS mission deployments. Each mission is briefly discussed and specific aspects regarding conditions or settings that impacted wave measurements are covered. Spectral estimates are given for each leg of the REMUS track plan to show how the measurements are impacted by the direction of vehicle travel.

D.1.1 April 20th 2012

The first REMUS mission to the MVCO was conducted on April 20th 2012. This first mission had three primary objectives.

The first objective was to determine if the REMUS ADCP would interfere or respond to the MVCO ADCP. To assess this interference, the REMUS drove circles of variable radius around the MVCO 12 meter node where the MVCO ADCP is installed. Post-processing showed no noticeable traces of interference in either the MVCO or REMUS ADCP water velocity records. It was determined that there would be no noticeable interference between the two sensors and that future data analysis did not require testing for interference.

The second objective was to deploy the Datawell Waverider buoy in the vicinity of

the MVCO. The buoy was deployed using the mooring configuration given in Figure 3-5 and was successfully deployed without any problems.

The third objective was to drive a rectangular path around the 12 meter node to get a better feel for the terrain topography around the MVCO ADCP and to verify the sampling settings of the ADCP. This information was used for future mission planning to determine an effective track length and vehicle speed for accurate wave measurements. The ADCP was initially configured to use twenty 25 cm bins. This configuration yielded a sample rate of only 1.38 Hz. The sample rate is directly linked to the number of bins, so the number of bins was reduced to 15 and the bin size increased to 35 cm for future deployments in an attempt to increase the sample rate closer to the MVCO rate of 2 Hz.

Due to the low sample rate and limited number of directional legs, the ADCP data from this mission was not used for wave analysis.

D.1.2 April 26th 2012

3DM software integration was completed just prior to the April 26th mission. The software was installed and the sensor was tested in the vehicle with good results. However, following the mission the sensor readings indicated that the 3DM had faulty accelerometers. The unit was removed from the vehicle and returned to Microstrain for repairs.

The rest of the REMUS systems performed exceptionally well. The change in number of bins from 20 to 15 increased the ADCP sample rate to 1.89 Hz and the north/south vehicle legs were increased to 1000 meters. The ADCP settings and mission track was used for all future missions.

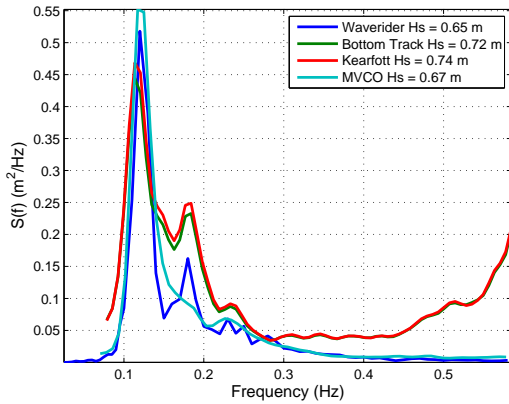
Wave Height Spectra

The height spectra for the four directional legs driven during the April 26th mission are given in Figure D-1.

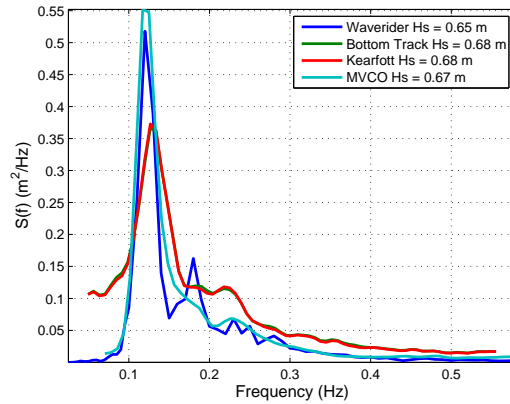
The spectral peaks for all of the directional legs correlate well with the wave buoy

and MVCO measurements. The significant height estimates are inflated slightly due to the peaks around .18 Hz. This peak is seen in the wave buoy estimate which indicate that it is a real wave signal and not an artifact generated by the REMUS measurements.

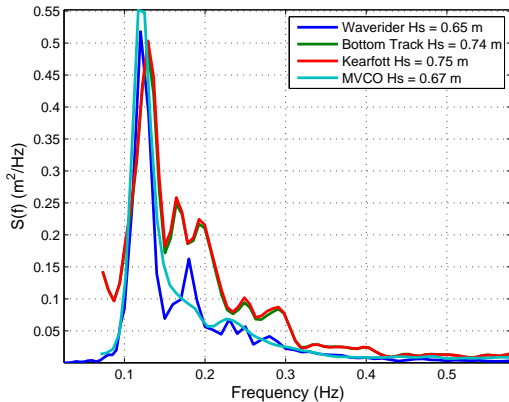
Recall that the significant wave height estimates are equal to four times the square root of the integral of the height spectrum. The height spectra are integrated from 0.1 to 0.3 Hz to limit low and high frequency noise from corrupting the estimates.



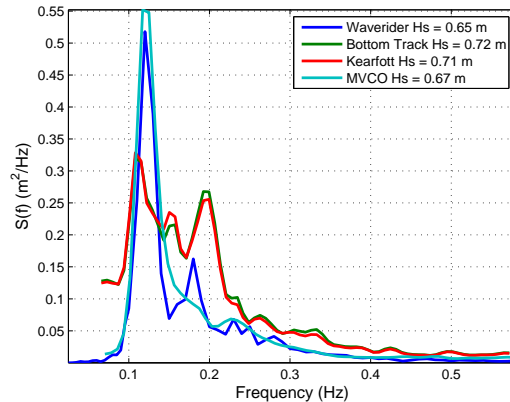
(a) Height spectrum during northern legs



(b) Height spectrum during southern legs



(c) Height spectrum during eastern legs



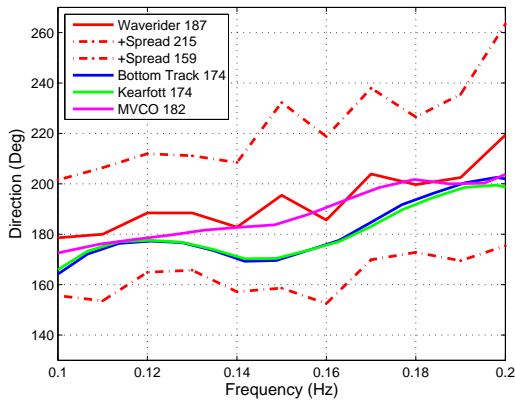
(d) Height spectrum during western legs

Figure D-1: These plots show the estimated height spectra and significant wave height from all of the employed sensors during the April 26th Mission.

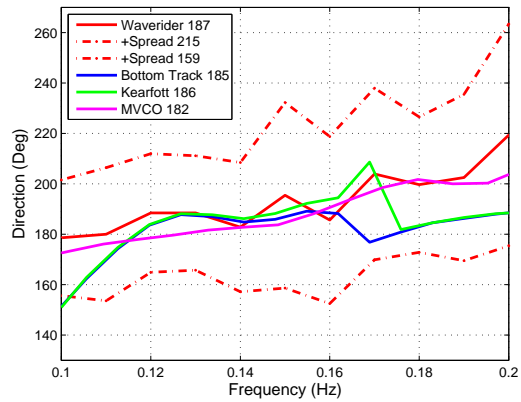
Mean Wave Direction

The mean wave directional estimates for the four directional legs driven during the April 26th mission are given in Figure D-2.

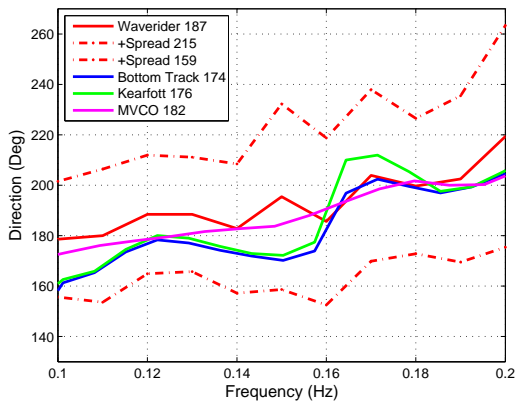
The mean direction estimates of the MVCO ADCP and REMUS are all within the estimated spread given by the wave buoy.



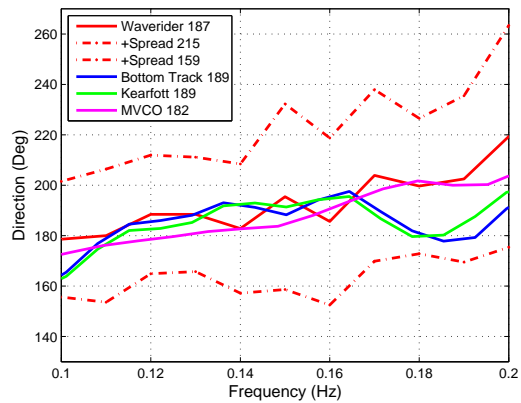
(a) Mean wave direction during northern legs



(b) Mean wave direction during southern legs



(c) Mean wave direction during eastern legs



(d) Mean wave direction during western legs

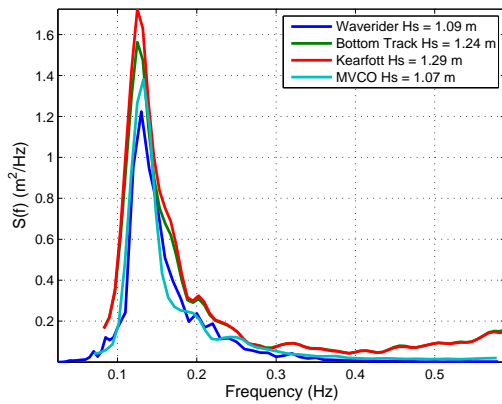
Figure D-2: These plots show the estimated mean wave direction from all of the employed sensors during the April 26th Mission.

D.1.3 May 17th 2012

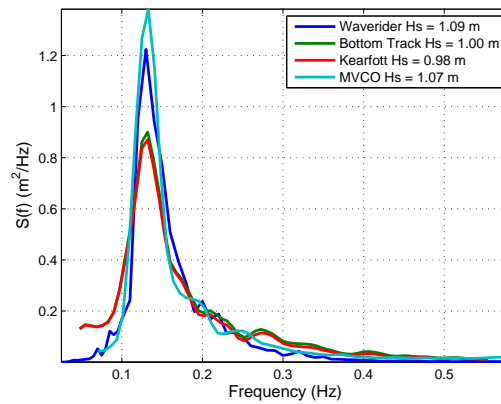
Due to its installation location inside the vehicle, the 3DM magnetometers were heavily biased by the magnetic field of the REMUS motor, resulting in unusable 3DM data. All other REMUS sensors were employed for ADCP velocity corrections.

Wave Height Spectra

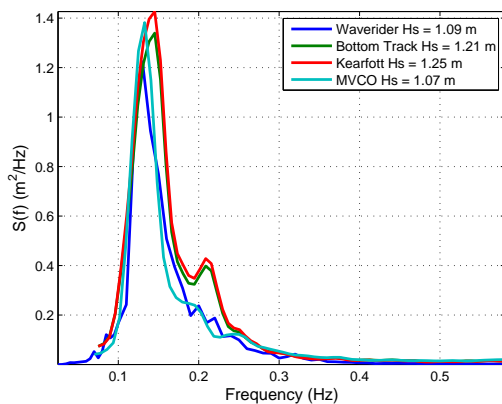
The height spectra for the four directional legs driven during the May 17th mission are given in Figure D-3.



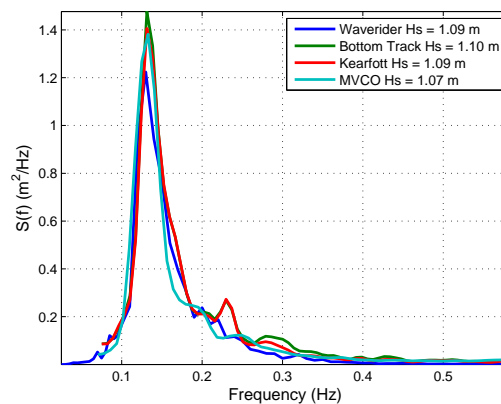
(a) Height spectrum during northern legs



(b) Height spectrum during southern legs



(c) Height spectrum during eastern legs



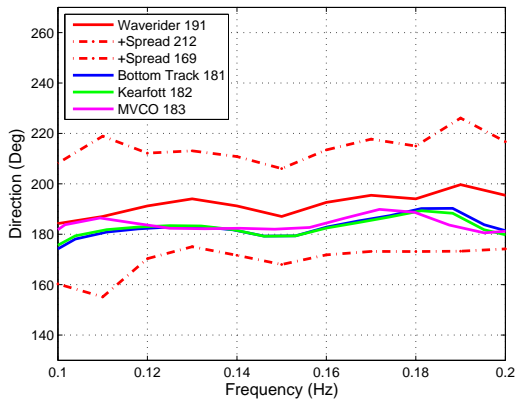
(d) Height spectrum during western legs

Figure D-3: These plots show the estimated height spectra and significant wave height from all of the employed sensors during the May 17th Mission.

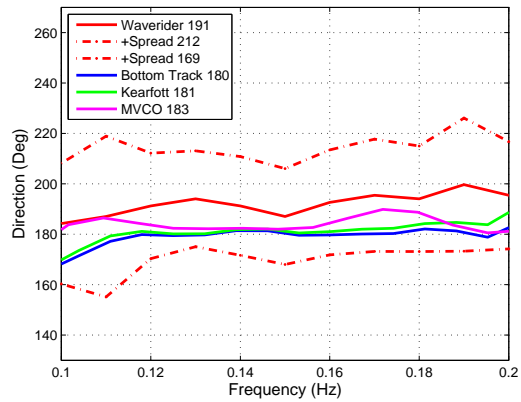
Mean Wave Direction

The mean wave directional estimates for the four directional legs driven during the May 17th mission are given in Figure D-4.

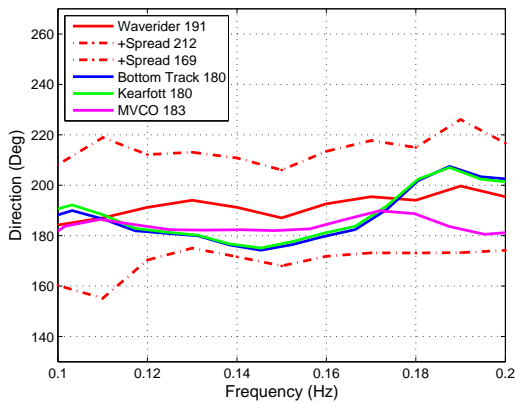
The REMUS corrected directions are off by an average of 10 degrees with the western leg showing the largest offset.



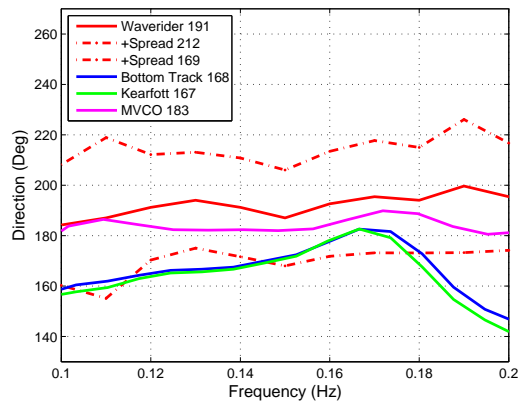
(a) Mean wave direction during northern legs



(b) Mean wave direction during southern legs



(c) Mean wave direction during eastern legs



(d) Mean wave direction during western legs

Figure D-4: These plots show the estimated mean wave direction from all of the employed sensors during the May 17th Mission.

D.1.4 July 27th 2012

The July 27th mission was the last mission for this research and the last attempt at obtaining a quality 3DM data set. The 3DM sensor was moved to the forward part of the REMUS vehicle to prevent biasing from the REMUS motor. Additionally, the 3DM was programmed to stream the CC data type that included the sensor rotation matrix in addition to the previously recorded accelerometer, angular rate, and magnetometer data. This allowed us to rotate and level the 3DM accelerometers using angles obtained at the same sample rate as the accelerometers, reducing the error in the integrated velocity measurements.

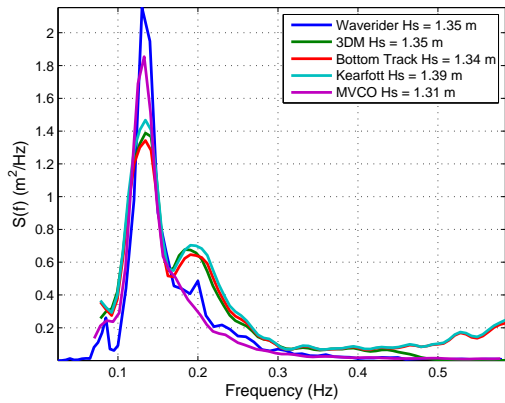
Wave Height Spectra

The height spectra for the four directional legs driven during the July 27th mission are given in Figure D-5.

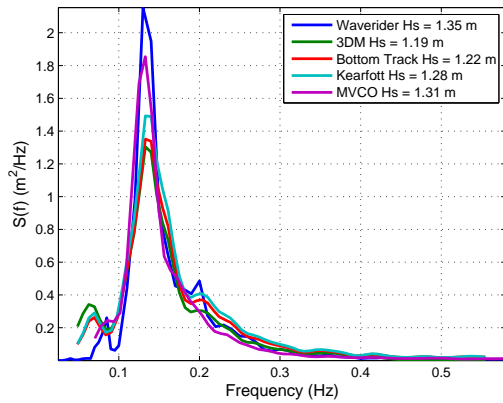
The height spectra and significant wave height estimates again agree well during the four different directional legs. The 0.2 Hz signal is again present during the northern and western legs, causing a slight over estimate of significant wave height in these directions.

Mean Wave Direction

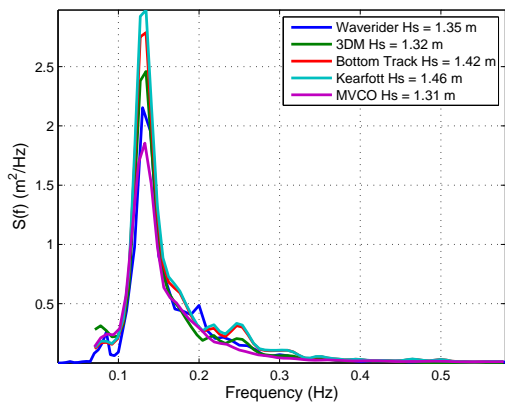
The mean wave directional estimates for the four directional legs driven during the July 27th mission are given in Figure D-6. The offset between the REMUS corrected measurements and the wave buoy have increased to an average of 14 degrees. The 3DM directional estimates are a bit more erratic, showing better results on the longer north and south legs.



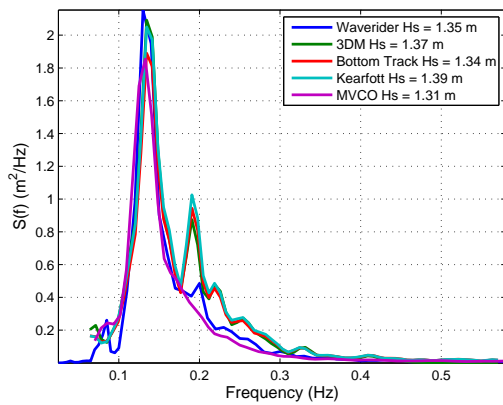
(a) Height spectrum during northern legs



(b) Height spectrum during southern legs

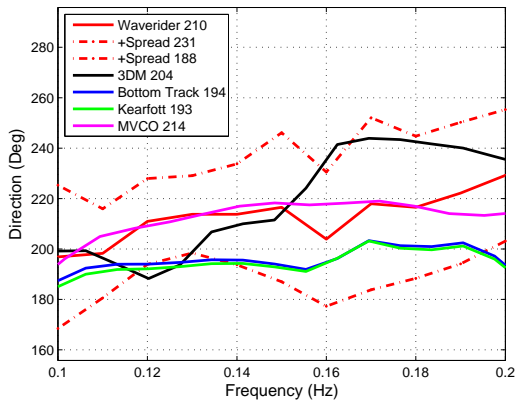


(c) Height spectrum during eastern legs

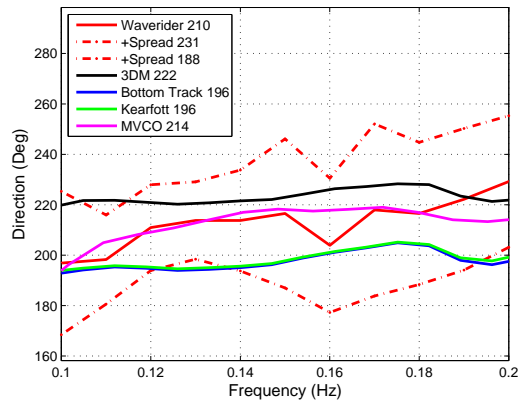


(d) Height spectrum during western legs

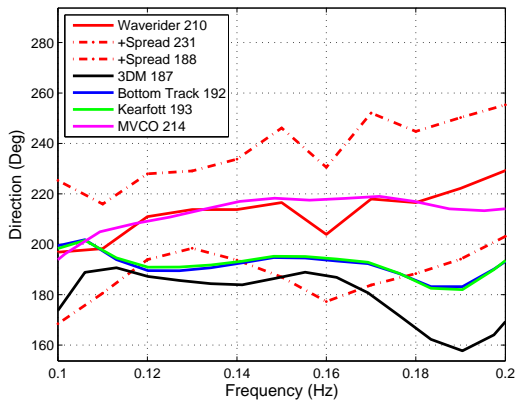
Figure D-5: These plots show the estimated height spectra and significant wave height from all of the employed sensors during the July 27th Mission.



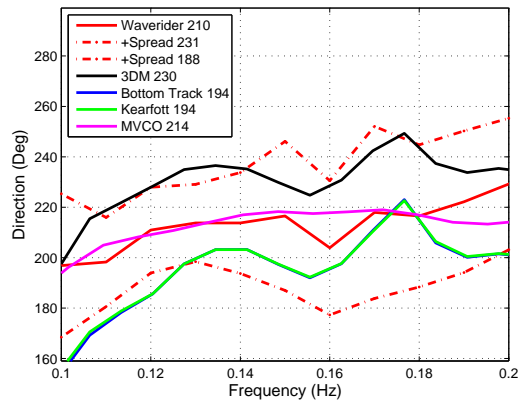
(a) Mean wave direction during northern legs



(b) Mean wave direction during southern legs



(c) Mean wave direction during eastern legs



(d) Mean wave direction during western legs

Figure D-6: These plots show the estimated mean wave direction from all of the employed sensors during the July 27th Mission.

Appendix E

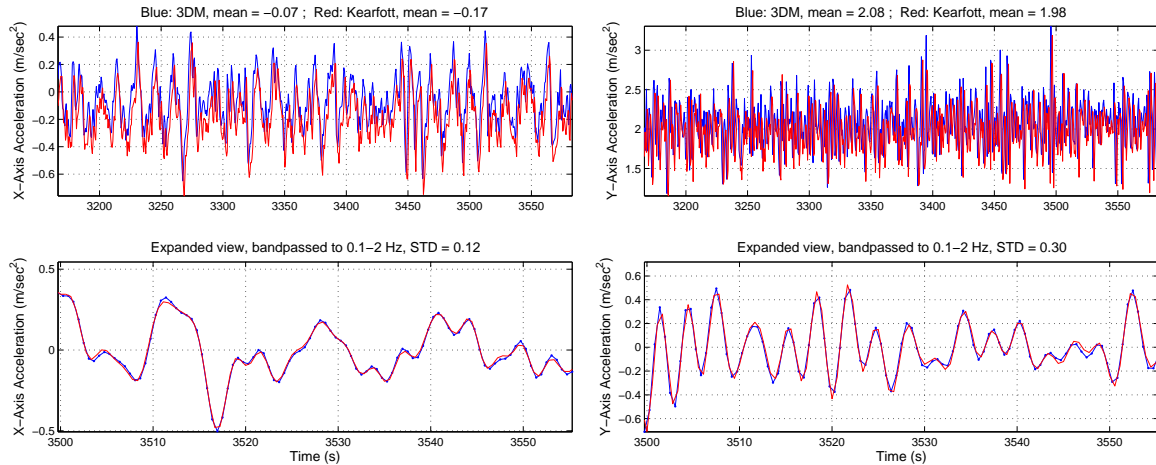
Additional Sensor Comparison Results

E.1 Introduction

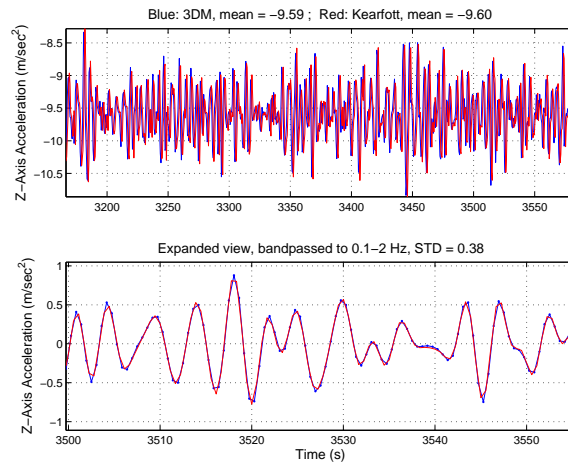
This section provides additional results from the comparison of sensor channels. Included are comparisons of all three accelerometer channels, angular rate channels, velocity channels, and pitch, roll, and heading channels. All of these signal comparisons are from data taken during the July 27 mission. This mission allowed for the most accurate 3DM measurements as the 3DM rotation matrix was directly streamed at a higher sample rate.

E.2 3DM to Kearfott Accelerometers

The 3DM and Kearfott accelerometer signals are shown in Figure E-1 and show excellent signal correlation. The 3DM accelerometers are used to determine the attitude of the sensor, as well as used to determine the vehicle velocities. The signal correlation in the wave band is particularly impressive.



(a) X-Axis Accelerometer 3DM to Kearfott Comparison (b) Y-Axis Accelerometer 3DM to Kearfott Comparison

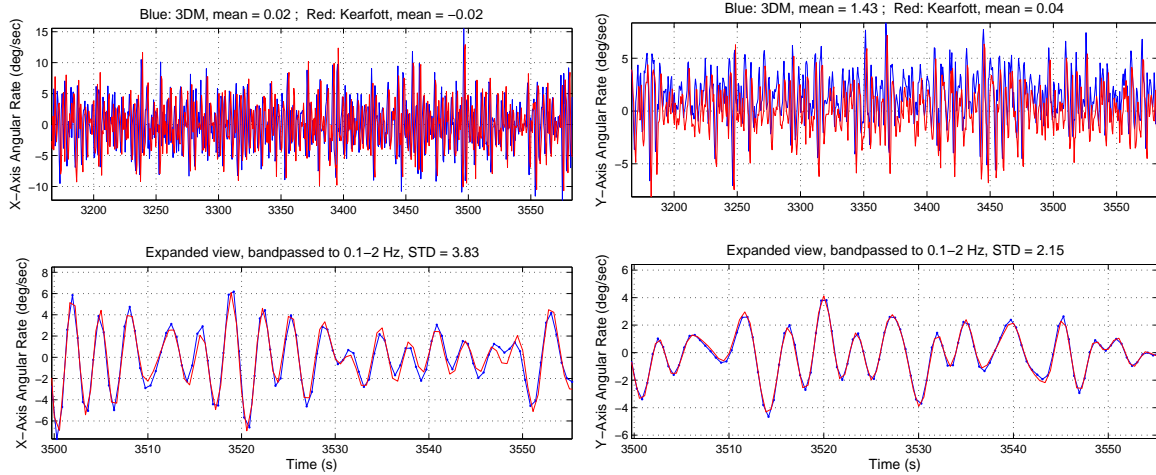


(c) Z-Axis Accelerometer 3DM to Kearfott Comparison

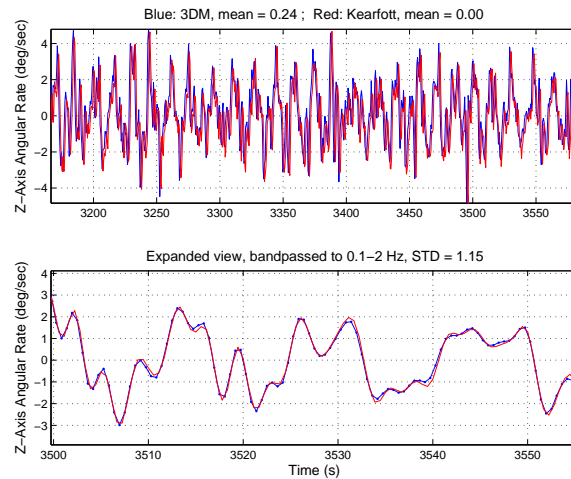
Figure E-1: These plots show the 3-axis accelerometer measurements from the 3DM and Kearfott sensors

E.3 3DM to Kearfott Angular Rates

The 3DM and Kearfott angular rate signals are shown in Figure E-2 and also show excellent signal correlation. The angular rate signals are used in conjunction with the accelerometer signals to determine the correct attitude of the sensor. They are combined using a complementary filter. The complementary filter is discussed in Appendix F.



(a) X-Axis Angular Rate 3DM to Kearfott Comparison (b) Y-Axis Angular Rate 3DM to Kearfott Comparison



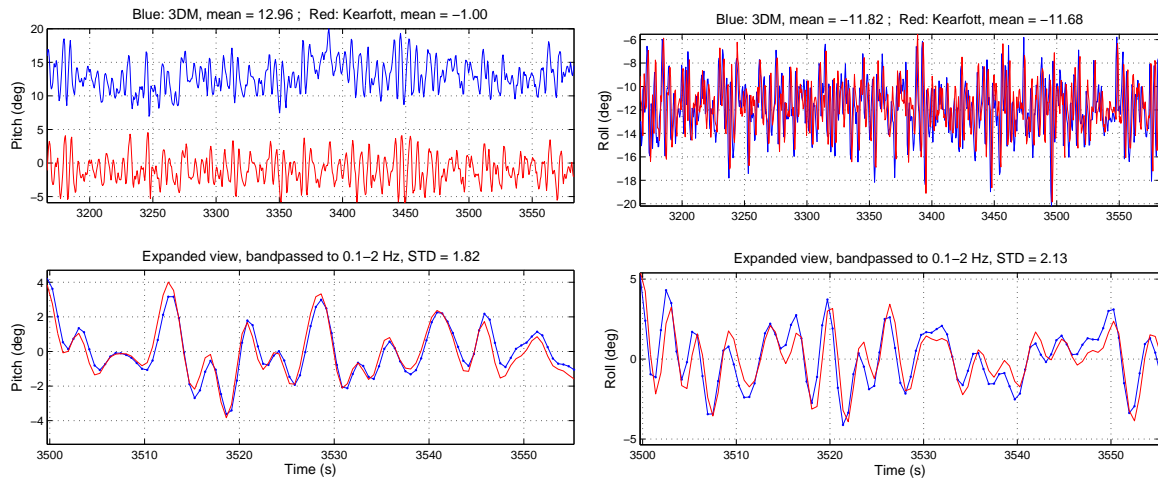
(c) Z-Axis Angular Rate 3DM to Kearfott Comparison

Figure E-2: These plots show the 3-axis angular rate measurements from the 3DM and Kearfott sensors

E.4 3DM to Kearfott Euler Angles

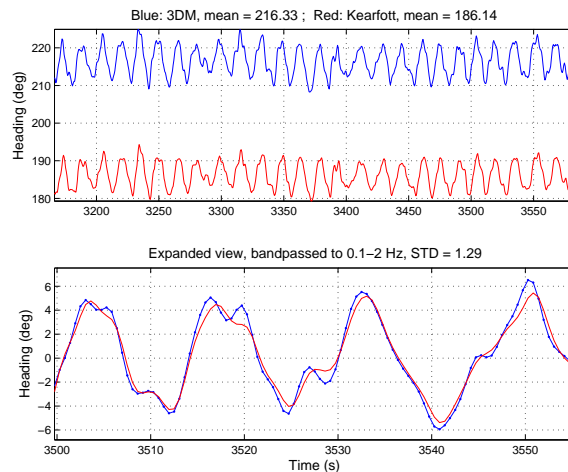
The 3DM and Kearfott euler angle signals are shown in Figure E-3. Because the raw accelerometer and angular rates show such good agreement in the wave band, the euler angles should also show great agreement in the wave band. While there are large offsets in the mean values of the pitch and heading, all three euler angles agree well in the wave band with some small fluctuations. Some of the offsets are discussed

in the discussion on 3DM sensor noise in Appendix F.



(a) Pitch 3DM to Kearfott Comparison

(b) Roll 3DM to Kearfott Comparison



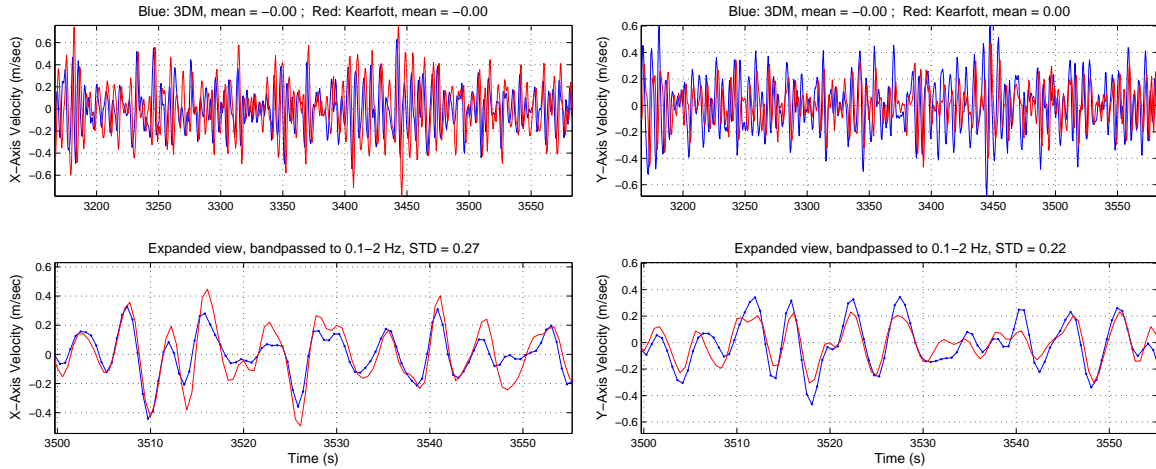
(c) Heading 3DM to Kearfott Comparison

Figure E-3: These plots show the euler angle measurements from the 3DM and Kearfott sensors

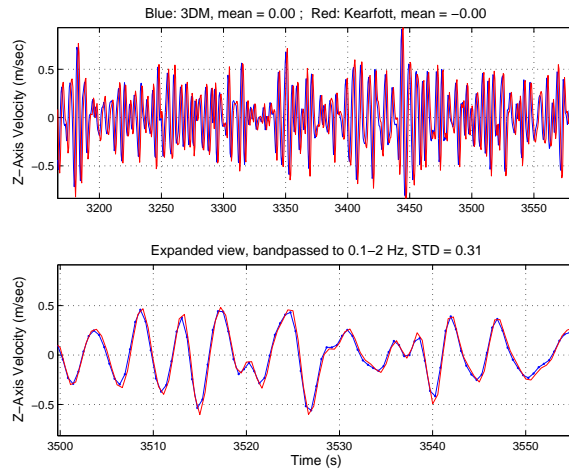
E.5 3DM to Kearfott Vehicle Velocities

The 3DM velocities shown are developed by first leveling the accelerometers into the Earth’s coordinate frame and then high-pass filtering the accelerometer signals to remove low frequency noise. The signals are then integrated to obtain the vehicle velocities in the Earth’s fixed coordinate system. Improving the performance of the

3DM through better sampling settings and calibration can improve the accuracy of these velocities.



(a) X-Axis 3DM to Kearfott Velocity Comparison (b) Y-Axis 3DM to Kearfott Velocity Comparison

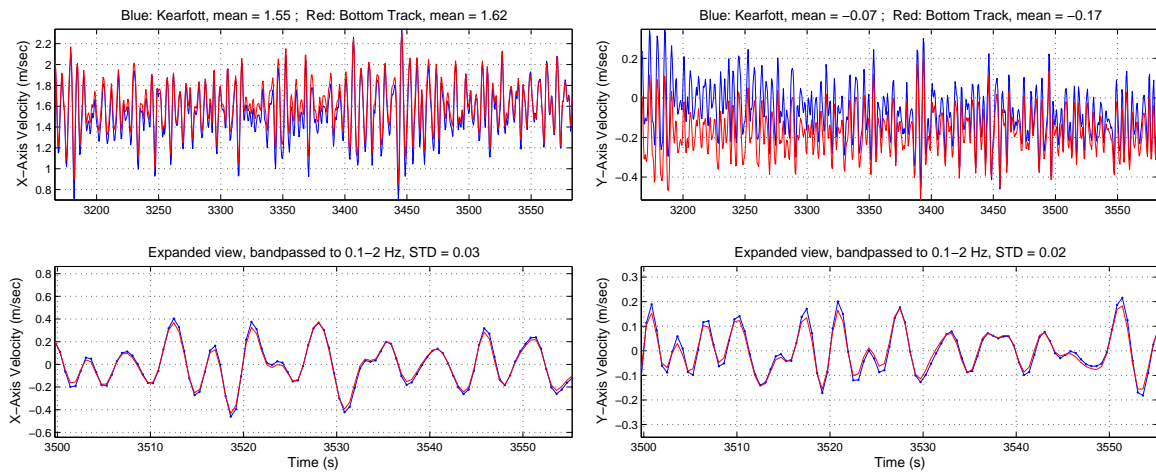


(c) Z-Axis 3DM to Kearfott Velocity Comparison

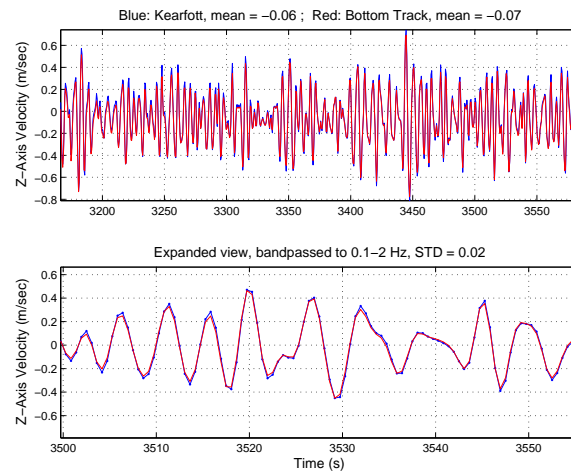
Figure E-4: These plots show the vehicle velocity measurements from the 3DM and Kearfott sensors

E.6 ADCP Bottom Track to Kearfott Vehicle Velocities

The ADCP bottom track and Kearfott vehicle velocity signals are shown in Figure E-5.



(a) X-Axis Bottom Track to Kearfott Velocity Comparison (b) Y-Axis Bottom Track to Kearfott Velocity Comparison



(c) Z-Axis Bottom Track to Kearfott Velocity Comparison

Figure E-5: These plots show the vehicle velocity measurements from the Kearfott and ADCP Bottom Track.

Appendix F

Microstrain Complementary Filter and Noise Analysis

F.1 Introduction

The Microstrain 3DM-GX3-25 uses a complementary filter to transform the angular rates and accelerations measured by the device into accurate heading and attitude information. Using the accelerometers or angular rates alone to determine attitude is inaccurate because accelerometers are unable to distinguish between actual accelerations and tilts and the inherent drift present in gyroscopes leads to large errors during numerical integration.

By low-pass filtering the accelerations and high-pass filtering the integrated angular rates, the data can be combined to produce accurate attitude and heading data over a wide range of frequencies.

F.2 Complementary Filter

The complementary filter used in the 3DM uses a combination of single pole low-pass and high-pass filters. The transfer functions of these filters are modeled by $L(\omega)$ and $H(\omega)$, respectively, where

$$L(\omega) = \frac{1}{1 + i\omega\tau} \quad (\text{F.1})$$

$$H(\omega) = \frac{i\omega\tau}{1 + i\omega\tau} \quad (\text{F.2})$$

ω is the radian frequency and τ defines the 3dB point of the filter.

The high-pass filter is applied to the angular rates while the low-pass filter is applied to the accelerometers. The complementary filter combines these two results based on the property that $L + H = 1$. The resulting estimate of angle is then a combination of the accelerometer-derived angle at low frequencies and angular rate-derived angle at high frequencies, with a combination of the two estimates at frequencies in between.

F.3 Sensor Noise and Error

Noise in the rate gyros and accelerometers combine in the complementary filter to create a random error in the attitude estimates. Additionally, bias is introduced into the angle estimate from the residual accelerometer signal in the waveband. To minimize this bias, the time constant of the filter, τ , was chosen to be 32 s in order to minimize the accelerometer signal in the band of wave frequencies. This has the undesirable effect of enhancing the error at low frequency due to gyro noise. However, we show that the errors in the wave band due to noise in both the accelerometers and rate gyros are small compared to the ‘bias’ error of the accelerometer signal leakage through the complementary filter.

We first address the random error due to sensor noise. In the following discussion, noise in the accelerometer and rate gyro are denoted by n_a and n_g , respectively, and the noise spectra are denoted by N_a and N_g .

The estimate of the angle generated by integrating the rate gyro is given by

$$\theta_g = \Omega/i\omega = \theta + n_g/i\omega \quad (\text{F.3})$$

where Ω is the angular rate in frequency space.

Similarly an estimate of angle from the accelerometer is given by

$$\theta_a = a = \theta + n_a \quad (\text{F.4})$$

where a the measured acceleration in frequency space in units of the gravitational acceleration, g .

We combine these using L and H to give the estimate of angle, $\hat{\theta}$, as

$$\hat{\theta} = \theta + L \cdot n_a + H \cdot n_g / i\omega = \theta + \frac{n_a + \tau n_g}{1 + i\omega\tau} \quad (\text{F.5})$$

The random error in angle, ϵ , can then be expressed as

$$\epsilon = \hat{\theta} - \theta = \frac{n_a + \tau n_g}{1 + i\omega\tau} \quad (\text{F.6})$$

Assuming that the accelerometer and rate gyro noises are uncorrelated, the power spectrum of the error is

$$S_\epsilon(\omega) = \frac{N_a + N_g \tau^2}{1 + (\omega\tau)^2} \quad (\text{F.7})$$

F.4 Static Lab Noise Analysis

Data was taken with the 3DM leveled (using a digital level) and stationary using the settings listed in table 3.4. Spectral analysis was used to determine the inherent noise present in the sensors and their contributions to the errors in the resulting attitude estimates.

Figure F-1 shows the spectrum of the x-axis accelerometer noise, N_a , (corresponding to roll), and the noise in the roll rate-gyro, $N_g \tau^2$.

Figure F-2 and F-3 compare the spectra of the 3DM pitch and roll outputs to the estimated error using the model presented in (F.7). The model and attitude error show strong agreement over a wide range of frequencies above the 3dB crossover point of the complementary filter. The agreement is especially good in the wave band

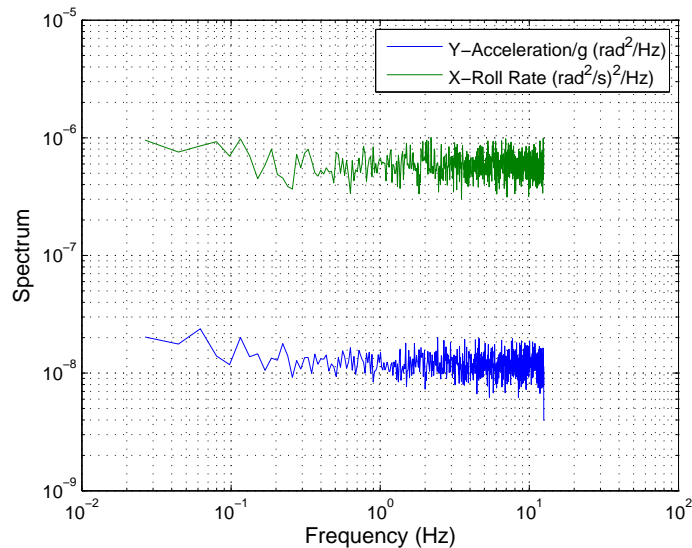


Figure F-1: This figure shows the 3DM x-axis accelerometer and roll rate gyro noise spectra taken from the 3DM during static testing in the lab.

indicating that the model is an accurate representation of the contribution of sensor noise to the estimation of attitude in those frequencies.

The noise level in the roll rate-gyro is $Ng < 10^{-6} \text{ (rad/s)}^2/\text{Hz}$. Defining the “wave band” to be frequencies in the range of 0.1 to 1 Hz, and integrating the model (F.7) over this range gives an *rms* error in roll of $\sigma_\theta \sim 0.03^\circ$ due to sensor noise. A similar value is found for the *rms* pitch error. We note in the next section that *rms* values of the measured AUV pitch and roll in the wave band were around 2° , so that the uncertainty in attitude due to sensor noise is on the order of 1 – 2 percent in the wave band.

F.5 Field Data Noise Analysis

Next we consider the acceleration bias. Data taken from the July 27th REMUS mission was analyzed to determine the bias generated by accelerometer signal leakage through the complementary filter. By comparing the measured *rms* pitch and roll in the wave band to the *rms* apparent tilt in the band inferred from the low-pass filtered accelerometer signal, we can estimate the percent error induced by the accelerometer

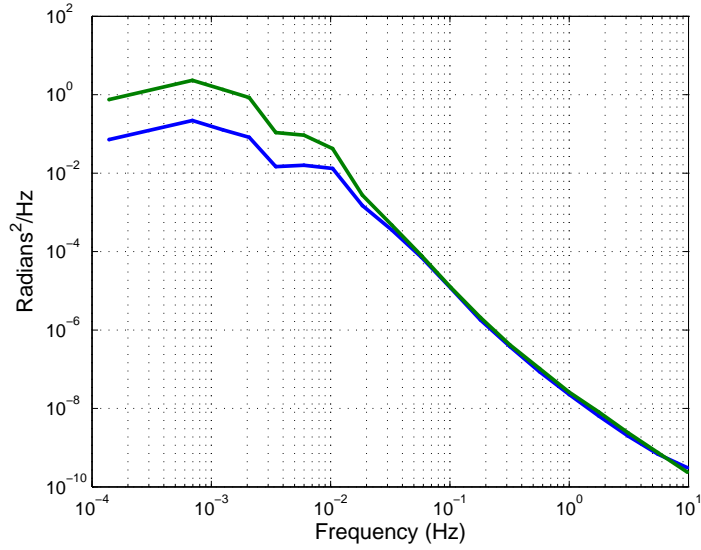


Figure F-2: This figure shows the 3DM pitch noise spectrum and the model (F.7) for the output of the complementary filter for pitch.

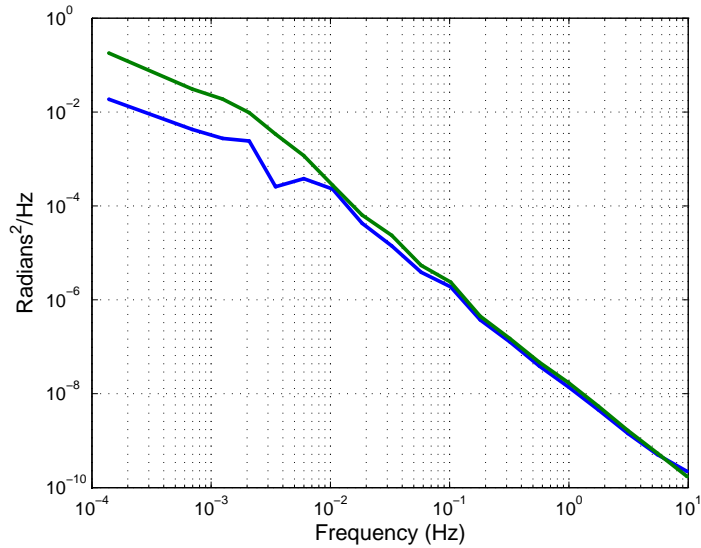


Figure F-3: This figure shows the 3DM roll noise spectrum and the model (F.7) for the output of the complementary filter for roll.

signal leakage.

The *rms* values of the 3DM pitch and roll in the wave band are determined by integrating the pitch and roll spectra over that range of frequencies. Similarly, the accelerometer signals are low-passed using the filter shown in (F.1) and the resulting spectra are integrated over the same band.

The resulting *rms* pitch and roll values were 2.2° and 2.0° , respectively. The corresponding *rms* accelerometer errors were 0.15° and 0.27° . These results show that the bias error due to accelerometer leakage through the complementary filter is in the range 7 to 13 % of the observed wave-driven tilts.

The amount of accelerometer leakage is determined by the time constant of the complementary filter. Our analysis concludes that acceleration bias is much more significant than sensor noise, so that for this application an even larger value of τ might be useful. However, much larger values of τ will affect the low frequency error in tilt, and more detailed modeling is required to select the optimal value of the time constant.

Bibliography

- Barber, N. F. and F. Ursell, “The generation and propagation of ocean waves and swell. I. Wave periods and velocities,” *Philosophical Transactions of the Royal Society of London. Series A, Mathematical and Physical Sciences*, vol. 240, no. 824, pp. pp. 527–560, 1948. [Online]. Available: <http://www.jstor.org/stable/91425>
- Barreira, L. and C. Ribeiro, “ADCP’s gravity waves data processing with wavelet matched phase method,” in *OCEANS 2011*, sept. 2011, pp. 1 –5.
- Brumley, B., R. Cabrera, K. Deines, and E. Terray, “Performance of a broad-band acoustic Doppler current profiler,” *Oceanic Engineering, IEEE Journal of*, vol. 16, no. 4, pp. 402 –407, oct 1991.
- Datawell Waverider Reference Manual*, Datawell, July 2010.
- Dean, R. G. and R. A. Dalrymple, *Water Wave Mechanics for Engineers and Scientists*. World Scientific, 1991.
- Donelan, M. A., W. M. Drennan, and A. K. Magnusson, “Nonstationary analysis of the directional properties of propagating waves,” *J. Phys. Oceanogr.*, vol. 26, pp. 1,901–1,914, 1996.
- Doucette, J. (2010) Martha’s vineyard coastal observatory. [Online]. Available: http://www.whoi.edu/mvco/description/observ_enlarged.html
- Fong, D. A. and N. L. Jones, “Evaluation of AUV-based ADCP measurements,” *Limnol. Oceanogr.: Methods*, vol. 4, pp. 58–67, 2006.
- Fong, D. A. and S. G. Monismith, “Evaluation of the accuracy of a ship-mounted bottom-tracking ADCP in a nearshore coastal flow,” *J. Atmos. Oceanic Tech.*, vol. 21, pp. 1,121–1,128, 2004.
- Goodman, L., E. Levine, and Z. Wang, “Subsurface observations of surface waves from an autonomous underwater vehicle,” *Oceanic Engineering, IEEE Journal of*, vol. 35, no. 4, pp. 779 –784, oct. 2010.
- Gordon, R. L. *Acoustic Doppler Current Profiler Principles of Operation, A Practical Primer*. RD Instruments, 2011.

- Jeans, G., C. Primrose, N. Descusse, B. Strong, and P. van Weert, “A comparison between directional wave measurements from the RDI Workhorse with Waves and the Datawell directional Waverider,” in *Current Measurement Technology, 2003. Proceedings of the IEEE/OES Seventh Working Conference on*, march 2003, pp. 148 – 151.
- Krogstad, H. E. and O. Arntsen, “Linear wave theory; Part A regular waves,” February 2000.
- Krogstad, H. E., R. L. Gordon, and M. C. Miller, “High-resolution directional wave spectra from horizontally mounted acoustic doppler current meters,” *J. Atmos. Oceanic Tech.*, vol. 5, pp. 340–352, 1988.
- Krogstad, H. E., A. K. Magnusson, and M. A. Donelan, “Wavelet and local directional analysis of ocean waves,” *Int. J. Offshore and Polar Engineering*, vol. 16, pp. 97–103, 2006.
- Kundu, P. K. *Fluid Mechanics*. Academic Press, Inc, 1990.
- Long, R. B. “The statistical evaluation of directional spectrum estimates derived from pitch/roll buoy data,” *J. Phys. Oceanogr.*, vol. 10, pp. 944–952, 1980.
- Longuet-Higgins, M. S. “On the statistical distribution of the heights of sea waves,” *J. of Marine Res.*, vol. 11, no. 3, pp. 245–266, 1952.
- , “The statistical analysis of a random, moving surface,” *Philosophical Transactions of the Royal Society of London. Series A, Mathematical and Physical Sciences*, vol. 249, no. 966, pp. pp. 321–387, 1957. [Online]. Available: <http://www.jstor.org/stable/91668>
- Longuet-Higgins, M. S., D. E. Cartwright, and N. D. Smith, *Ocean Wave Spectra*. Prentice-Hall, 1963, ch. Observations of the directional spectrum of sea waves using the motions of a floating buoy, pp. 111–136.
- Mettlach, T. and C.-C. Teng, “Concepts for an ideal ocean wave-measuring buoy,” in *OCEANS 2010*, sept. 2010, pp. 1 –8.
- Nagata, Y. “The statistical properties of orbital wave motions and their application for the measurement of directional wave spectra,” *J. Oceanogr. Soc. Japan*, vol. 19, pp. 169–181, 1964.
- Pinkel, R. and J. A. Smith, “Open ocean surface wave measurement using doppler sonar,” *J. Geophys. Res.*, vol. 92, pp. 12,967–12,973, 1987.
- Rice, S. O. “Mathematical analysis of random noise,” *Bell Systems Tech.J.*, vol. 23, pp. 282–332, 1944.
- Riedel, J. and A. Healey, “Shallow water station keeping of AUVs using multi-sensor fusion for wave disturbance prediction and compensation,” in *OCEANS ’98 Conference Proceedings*, vol. 2, sep-1 oct 1998, pp. 1064 –1068 vol.2.

- , “Estimation of directional wave spectra from an autonomous underwater vehicle,” Naval Warfare Tech. Report TRA-130634, Tech. Rep., 2005.
- Rowe, F. and J. Young, “An ocean current profiler using doppler sonar,” in *OCEANS '79*, sept. 1979, pp. 292 –297.
- Rowe, F., K. Deines, and R. Gordon, “High resolution current profiler,” in *Current Measurement, Proceedings of the 1986 IEEE Third Working Conference on*, vol. 3, jan 1986, pp. 184 – 189.
- Sharp, K. and R. White, “More tools in the toolbox: The Naval Oceanographic Office’s remote environmental monitoring units (REMUS) 6000 AUV,” in *OCEANS 2008*, sept. 2008, pp. 1 –4.
- Smith, J. A. “Doppler sonar and surface waves: range and resolution,” *J. Atmos. Oceanic Tech.*, vol. 6, pp. 680–696, 1989.
- Strong, B., B. Brumley, E. Terray, and G. Stone, “The performance of ADCP-derived directional wave spectra and comparison with other independent measurements,” in *OCEANS 2000 MTS/IEEE Conference and Exhibition*, vol. 2, 2000, pp. 1195 –1203 vol.2.
- ADCP Coordinate Transformation - Formulas and Calculations*, Teledyne RD Instruments, January 2008.
- Terray, E., R. Gordon, and B. Brumley, “Measuring wave height and direction using upward-looking ADCPs,” in *OCEANS '97. MTS/IEEE Conference Proceedings*, vol. 1, oct 1997, pp. 287 –290 vol.1.
- Terray, E., H. Krogstad, P. Cabrera, R. Gordon, and A. Lohrmann, “Measuring wave direction using upward-looking doppler sonar,” in *Current Measurement, 1990., Proceedings of the IEEE Fourth Working Conference on*, apr 1990, pp. 252 –257.
- Trevorrow, M. V. and I. J. Booth, “Extraction of ocean wave directional spectra using steerable doppler side-scan sonars,” *J. Atmos. Oceanic Tech.*, vol. 12, pp. 1,087–1,100, 1995.
- Wood, J., E. Terray, B. Strong, and B. Singh, “Measurement of deepwater ocean waves from a subsurface mooring,” in *Oceans 2005 - Europe*, vol. 1, june 2005, pp. 166 – 171 Vol. 1.